COLORADO
Department of Transportation

CDOT Office of Applied Research

Quantification of Field Performance and Nondestructive Testing of Timber Bridges in Colorado

Yail Jimmy Kim

December 2024
CDOT-2024-04

Technical Report Documentation Page

1. Report No. CDOT-2024-04	2. Government Accession No.	3. Recipient's Catalog No.
4. Title and Subtitle Quantification of Field Performance and Nondestructive Testing of Timber Bridges in Colorado		5. Report Date 12/31/2024
		6. Performing Organization Code
7. Author(s) Yail Jimmy Kim		8. Performing Organization Report No.
9. Performing Organization Name and Address University of Colorado Denver 1200 Larimer St., Denver, CO 80217		10. Work Unit No. (TRAIS)
		11. Contract or Grant No.
12. Sponsoring Agency Name and Address Colorado Department of Transportation Office of Applied Research 2829 W. Howard Place Denver, CO 80204		13. Type of Report and Period Covered
		14. Sponsoring Agency Code

15. Supplementary Notes

Prepared in cooperation with the US Department of Transportation, Federal Highway Administration

16. Abstract

This report presents two major aspects related to evaluating timber bridges with nondestructive testing: i) laboratory experiments and ii) field applications. The first part of the report discusses the degradation processes and resulting outcomes of structural timber, Douglas Fir, that is broadly used for bridge construction. In accordance with the standard protocol of ASTM D1037, specimens are conditioned and their physical and mechanical properties are measured using nondestructive test methods: moisture metering, stress wave timing, and microdrilling. The second part of the report deals with the condition evaluation of timber bridges with the aim of synthesizing ratings from visual inspections (qualitative) and nondestructive testing (quantitative). Ten benchmark bridges, visually rated as Poor and Fair according to the scale of the Federal Highway Administration, are selected and their responses are examined by moisture metering, stress wave analysis, and microdrilling techniques for determining deterioration levels. A machine learning algorithm is trained and employed for comparative analysis, demonstrating that the integration of the two inspection approaches is achievable to improve the rating procedure for aged timber bridges. To implement Load and Resistance Factor Rating (LRFR), condition factors are calibrated and practice recommendations are suggested.

Implementation (Optional)
Nondestructive testing is implemented for the condition rating of timber bridges

17. Keywords bridges; deterioration; nondestructive testing; rating; timber	18. Distribution Statement This document is available on CDOT's website: https://www.codot.gov/programs/research

19. Security Classif. (of this report) Unclassified	20. Security Classif. (of this page) Unclassified	21. No. of Pages	22. Price

Form DOT F 1700.7 (8-72) Reproduction of completed page authorized

Acknowledgments

The research team would like to acknowledge valuable guidance and thought-provoking comments provided by Natasha Butler, Lynn Crosswell, and Michael Collins (Staff Bridge, CDOT). The research team is also grateful to Thien Tran (Applied Research and Innovation Branch, CDOT) for his comprehensive support and administrative assistance.

Executive Summary

This report presents two major aspects related to evaluating timber bridges with nondestructive testing: i) laboratory experiments and ii) field applications. The first part of the report discusses the degradation processes and resulting outcomes of structural timber, Douglas Fir, that is broadly used for bridge construction. In accordance with the standard protocol of ASTM D1037, specimens are conditioned and their physical and mechanical properties are measured using nondestructive test methods: moisture metering, stress wave timing, and microdrilling. Furthermore, rebound hammering and digital microscopy characterize the influence of progressive deterioration. After completing planned exposure cycles, all specimens are loaded until failure takes place and the consequences from the nondestructive and destructive tests are appraised comparatively. The accelerated aging causes anisotropic damage with longitudinal checks alongside a change in surface color from light brown to reddish brown. Within a fiber saturation point of 30%, moisture absorption gives rise to local swelling, raises splitting stresses, and enlarges cellular cavities. With an increase in the internal damage level, stress wave timing ascends by 63.5% and travel velocities declines by 38.8%. The resistance of microdrilling also alters from stable to multipeak patterns, representing hardened cell walls and collapsed lumens. A link is established for converting nondestructive metrics to deterioration ratios. Computational algorithms based on machine learning technologies predict the level of deterioration and are employed to formulate performance classifications for practical application.

The second part of the report deals with the condition evaluation of timber bridges with the aim of synthesizing ratings from visual inspections (qualitative) and nondestructive testing (quantitative). Ten benchmark bridges, visually rated as Poor and Fair according to the scale of the Federal Highway Administration, are selected and their responses are examined by moisture metering, stress wave analysis, and microdrilling techniques for determining deterioration levels. The moisture content of the bridges is also measured and a threshold value of 20% is confirmed to be an acceptable limit that distinguishes Poor and Fair conditions. The degree of internal damage influences the velocity of stress waves travelling through the bridge girders, with a magnitude below 4,467 ft/sec indicating a Poor condition. On the changes observed in stress wave timing, the Fair-rated bridges exhibit a stable pattern relative to the Poor-rated bridges manifesting a 194.8% higher coefficient of variation. When the bridge conditions decline, wave-timing values tend to rise above 2,408 microsec./ft. The drilling resistance of the Poor-rated bridges is over 31% lower than that of the Fair-rated bridges with a greater probability of being less than the baseline resistance of 70.7%. As far as deterioration levels are concerned, there are discrepancies between the results of the qualitative and quantitative methodologies for the Poor-rated bridges; however, consistent observations are made for the Fair-rated bridges. A machine learning algorithm is trained and employed for comparative analysis, demonstrating that the integration of the two inspection approaches is achievable to improve the rating procedure for aged timber bridges. To implement Load and Resistance Factor Rating (LRFR), condition factors are calibrated and practice recommendations are suggested.

Implementable Outcomes: a mean deterioration ratio (D_R = (Eqs. i + ii + iii)/3) is calculated using governing (maximum) deterioration ratios supplied by the three nondestructive test methods (Eqs. ia, iia, and iiia) at no less than ten randomly selected locations ($D_R \leq 30\%$: Fair and $30\% < D_R$: Poor) and then the consequences of visual inspections at the structural scale (e.g., physical damage) are synthesized to inform a rating decision.

$$D_R = 2.22\left(V_R\right)^{0.84} \qquad \text{(velocity)} \qquad \text{(i)}$$

$$V_R = \frac{\left(V_{cont} - V_{\det}\right)}{V_{cont}} \times 100 \text{ with } V_{det} \leq V_{cont} \qquad \text{(ia)}$$

(V_{cont} = 4,467 ft/sec and V_{det} = measured on site)

$$D_R = 3.9\left(W_R\right)^{0.59} \qquad \text{(wave timing)} \qquad \text{(ii)}$$

$$W_R = \frac{\left(W_{\det} - W_{cont}\right)}{W_{cont}} \times 100 \text{ with } W_{cont} \leq W_{det} \qquad \text{(iia)}$$

(W_{cont} = 2,408 microsec./ft and W_{det} = measured on site)

$$D_R = 26.8\left(R_R\right)^{0.075} \qquad \text{(drilling resistance)} \qquad \text{(iii)}$$

$$R_R = \frac{\left(R_{cont} - R_{\det}\right)}{R_{cont}} \times 100 \text{ with } R_{det} \leq R_{cont} \qquad \text{(iiia)}$$

(R_{cont} = 70.7% and R_{det} = measured on site)

Keywords: bridges; deterioration; field-testing; nondestructive testing; rating; timber

List of Tables

List of Figures

Table of Contents

Part I: Nondestructive and Destructive Tests for Damage Quantification of Deteriorated Structural Timber

I.1. Introduction

Wood has been instrumental as a means to build bridge structures before the era of contemporary construction materials. Between the 18th and 19th centuries, approximately 10,000 timber bridges were erected in the United States (Kromoser et al. 2024). The prevalence of timber bridges is noticeable in Colorado, Montana, Nebraska, and North Dakota (Radford et al. 2002). Given that timber is composed of organic substances, a number of causes downgrade the performance of timber bridges; for example, aging, aggressive environments, biological decays, and detrimental chemicals (Sundararaj 2022). Particularly, timber can be in a state of synergistic degeneration when randomly dispersed natural flaws are associated with excessive vehicle loadings (Rashidi et al. 2021); thus, transportation authorities allocate a substantial budget to maintain the quality of timber bridges (Fosnacht 2020). From a strategic perspective, timely inspections and ensuing technical actions are salient to save rehabilitation expenses and to prevent the catastrophic collapse of deficient bridges.

Nondestructive testing is a cost-effective solution when investigating the condition of structural members. Nondestructive testing provides numerous benefits (e.g., early damage detection, accurate outcome, convenient implementation, and broad applicability) and helps determine the in-situ properties, physical states, and ratings of timber bridges (Palma and Steiger 2020). By conducting nondestructive tests as part of a site inspection, bridge management programs are not reliant upon qualitative visual appraisals, but are established via data-driven protocols. Among many, emphasis may be placed on the succeeding techniques that are especially useful for bridge applications:

- Moisture metering—since moisture plays an important role in dominating the strength and elastic modulus of timber, moisture contents should be measured. It is reasonable to state that timber elements with a moisture content of 20% or higher are vulnerable to decay (USDA 2010); accordingly, preventive and corrective maintenance ought to be planned through properly monitored moisture contents: moisture control, grain treatment, capping, fumigant, connection checks, drainage, and epoxy injection, all of which can extend the service life of timber bridges (Dahlberg et al. 2015).

- Stress wave timing—stress waves are proven technology for detecting internal deterioration in timber bridges (Honfi et al. 2017). A wide range of decay caused by fungi, insects, and other detrimental factors is identified by a stress wave timer (Rashidi et al. 2021). Stress waves are equivalent to sound waves traveling across timber. The basic concept of the timer is that mechanical stress waves are generated across a timber element and responses are measured to examine the conditions and properties of the element. The propagation of the waves is rapid if an element possesses a high density without voids and decay. If a void exists, the signal transmission of stress waves becomes slow and hence the presence of internal decay is detected (Duquett 2021). The in-situ elastic modulus of timber may be determined as a function of density and wave propagation velocity. Considering that the sensitivity of a stress wave timer depends upon a service situation (Yu et al. 2017), other methods should be used together in order to raise the level of accuracy.
- Microdrilling—A tiny metallic needle-like core bit is drilled into timber and its resistance is recorded to estimate soundness (Cabaleiro et al. 2018). The operating principle of this test is that the electrical power consumption of a needle motor is converted to the mechanical torque of the needle (White and Ross 2014). Strictly speaking, micro-drilling is destructive; however, it is regarded as nondestructive because the degree of damage is negligible (Brashaw et al. 2015).

Although these nondestructive testing techniques are well recognized to be suitable (Palma and Steiger 2020), their adaptability along with destructive testing received limited attention for timber bridges. As such, obscure links exist between these disparate approaches, and intrinsic complexities stemming from empirical field inspections need to be addressed.

This research discusses the deterioration mechanisms of structural timber and quantified damage based on the aforementioned nondestructive test methods in parallel with destructive testing. An experimental program is carried out pursuant to the aging protocol of ASTM D1037 (ASTM 2020) that is commonly acknowledged as one of the most effective methods for replicating natural service environments (Wang et al. 2021). Furthermore, machine learning algorithms are utilized to supplement laboratory findings, which will lead to the development of practical inspection guidelines for constructed bridges.

I.2. Experimental Procedure

Outlined below is an overview of laboratory testing that consists of specimens, conditioning schemes, and experimental methodologies. Various instruments are applied to nondestructively diagnose the condition of degraded timber, which would be engaged with data from destructive assessments.

I.2.1. Material

A total of 40 Sustainable Forestry Initiative (SFI)-certified Douglas Fir beams were prepared with precut dimensions of 3.5 in. wide by 9.5 in. deep by 16 in. long. All SFI-certified lumber products are treated with minimal chemicals and independently evaluated by third parties to warrant quality and performance (SFI 2023). The nominal elastic modulus of the beams was expected to vary from E = 1,160 ksi to 1,940 ksi as per the USDA Wood Handbook (USDA 2010).

Table I.1. Accelerated aging protocol of ASTM D1037 (ASTM 2020)

Condition	Duration[a]	Purpose
Soaking (120 ± 3.6°F)	1 hour	Causing swelling
Steaming (199 ± 5.4°F)	3 hours	Degrading fibers
Freezing (10 ± 5.4°F)	20 hours	Simulating cold temperature exposure
Oven-drying (210 ± 3.6°F)	3 hours	Causing shrinkage and splitting
Steaming (199 ± 5.4°F)	3 hours	Degrading fibers
Oven-drying (210 ± 3.6°F)	18 hours	Causing shrinkage and splitting

[a]: one cycle

I.2.2. Conditioning

The beams were classified into two groups: Control (10 specimens) and Deteriorated (30 specimens). In accordance with the test protocol of ASTM D1037 (ASTM 2020), the specimens in the Deteriorated category were subjected to accelerated aging. Figure I.1(a) illustrates one cycle of conditioning with soaking, steaming, freezing, and oven-drying for 48 hours (Table I.1). These sequential steps were repeated six times, as stipulated in ASTM D1037 (ASTM 2020), and the properties of the timber were measured after one, three, and six cycles (10 specimens, each) to examine the progression of damage. Upon completion of the planned cycling, all specimens were stored in an environmental chamber (an average temperature of 68ºF at a relative humidity of 65%) for 48 hours (ASTM 2020). The conditioned beams were cleaned and surface moisture was wiped off, then ten locations were marked for laboratory testing (Fig. I.1(b)). Densities were also checked immediately after oven-drying during the scheduled conditioning intervals (without resting) and after a 48-hour settling period (with resting). The rationale for separately handling these two density groups was to study the moisture absorption capability of the deteriorated timber.

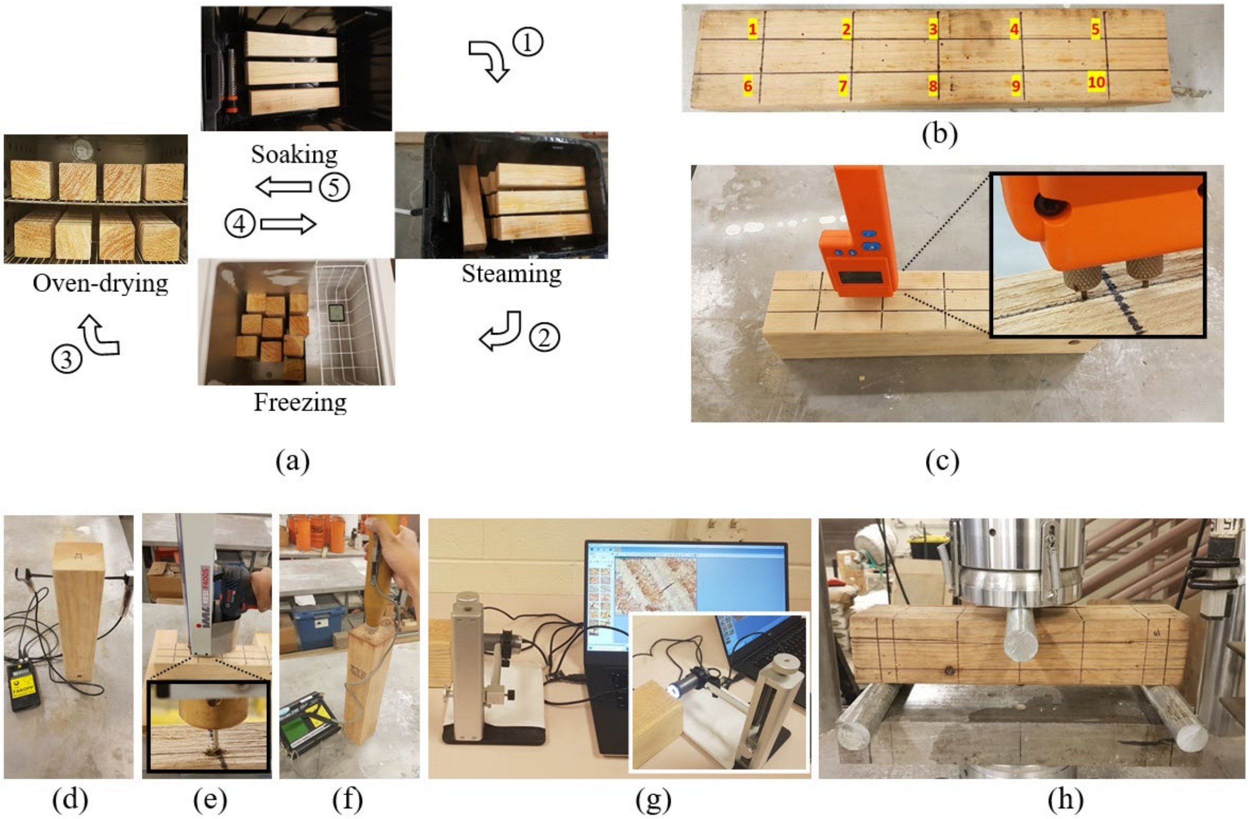

Fig. I.1. Test methods: (a) conditioning per ASTM D1037 (ASTM 2020); (b) position marking; (c) moisture meter; (d) stress wave timer; (e) microdrill; (f) rebound hammer; (g) digital microscopy; (h) three-point bending

I.2.3. Nondestructive testing

I.2.3.1. Moisture meter

A handheld moisture meter, comprising a digital readout and two contact pins with a penetration depth of 0.3 in., was used (Fig. I.1(c), inset). The range of gaugeable moisture contents was 6%

to 40% within an operating temperature range between 50ºF and 90ºF. This commercial device was calibrated by the manufacturer to accommodate over 50 timber species and a designated code was selected for Douglas Fir. To ensure the calibrated readings of the moisture meter, an ancillary test was undertaken independently (details will follow). As pictured in Fig. I.1(c), the moisture contents of the specimens were logged at each of the marked locations.

I.2.3.2. Stress wave timer

The soundness of the specimens was assessed by a stress wave timer. The device generates ultrasound at a frequency range of 15 kHz to 300 kHz and a time resolution of ±1 microsec. within an operating temperature of 32ºF to 95ºF. A pair of piezoelectric transducers (0.5 in. in diameter and 1.1 in. in length) was pierced to a depth of 0.5 in. (Fig. I.1(d)) and an excitation force was exerted by a steel hammer on one of the transducers (exciter) to produce wave signals, which were sensed by the other (receiver). A preliminary task was performed to establish a relationship between transit times and transducer spacings, and a distance of 3.5 in. was selected for the transducers. Afterward, the travel time and velocity of stress waves were recorded to quantify the condition of the control and deteriorated specimens.

I.2.3.3. Microdrill

A cordless microdrill was employed with a bit diameter of 0.12 in. and a maximum drilling depth of 16 in. at a feed speed of up to 1 in. /sec. The core bit was placed perpendicular to the timber surface at the marked positions (Fig. I.1(e)) and the resistance of the specimens, which was explained earlier in the context of a mechanical torque, was measured. Test results were transmitted to a data acquisition unit through Bluetooth technology.

I.2.3.4. Rebound hammer

In line with the resistance of microdrilling, rebound hammering was carried out to figure out the near-surface hardness of the timber (Fig. I.1(f)). The device was equipped with a mechanical mass and springs that characterized the variation of kinetic energy before and after impact for the calculation of a rebound number; subsequently, the number was converted to compressive strength using a regression formula calibrated by the manufacturer (Kumavat et al. 2021).

I.2.3.5. Digital microscopy

The exterior texture of the control and deteriorated specimens was inspected by a digital microscope (Fig. I.1(g)). The instrument is a polarized light type, built with a complementary metal oxide semiconductor (CMOS) sensor, and furnishes 1,280 × 1,024 pixel images at a rate of 30 frames per second.

I.2.4. Destructive testing

For measuring the modulus of elasticity, modulus of rupture, and ultimate capacity of the specimens, three-point bending was applied (Fig. I.1(h)). The beams were simply supported with a span length of 13.8 in. and were monotonically loaded at a rate of 0.1 in./min until failure occurred, as guided by ASTM D198 (ASTM 2015). A load cell and a linear potentiometer monitored the load and displacement at midspan, respectively.

I.3. Test Results

This section elaborates on experimental observations and quantitative information as regards the physical and mechanical characteristics of intact and aged timber specimens. Both nondestructive and destructive test outcomes are delineated and their reciprocal dependency is emphasized.

I.3.1. Qualitative assessment

The macroscopic view of the control and deteriorated (three cycles) specimens is shown in Figs. I.2(a) and (b), respectively. The accelerated aging of the timber darkened its surface from light brown (Fig. I.2(a)) to reddish brown (Fig. I.2(b)), which can be attributed to the interactions between cell lumens and water molecules in tandem with hydrogen bonds and capillary condensation (Baar et al. 2019). After conditioning, anisotropic damage was noticed with multiple checks in the longitudinal direction (Fig. I.2(b)). Figure I.2(c) exhibits microscopic images of the control specimen at 20 and 100 times magnifications. The scanned topography indicates the presence of periodic cell walls without biological flaws. The evolutionary degradation of the deteriorated specimens is visible in Figs. I.2(d) to (f). A decrease in amorphous cellulose and hemicellulose components was responsible for the heterogeneous degradation, entailing the crumpling, cracking, and delamination of the cell walls (Kacik et al. 2014; Xin et al. 2022). For the specimen suffering one cycle (Fig. I.2(d)), the absorption of moisture caused local swelling and raised splitting stresses that exceeded the cohesive strength of tracheids (Deng et al. 2024); consequently, alternate cracks initiated and progressed, which would reduce the modulus of rupture (to be revisited). With an increase in the conditioning to three cycles (Fig. I.2(e)), the level of deterioration was exacerbated and the configuration of the microstructure was remarkably transformed. The repeated expansion and contraction processes during the cycling expedited the splitting of intercellular spaces (Smith et al. 2003); scilicet, the coalescent dislocations of the cell structure (i.e., connected discrete cracks in the weak planes of the grains) precipitated irreversible damage in the specimen. As the specimen underwent six cycles (Fig. I.2(f)), irregular deterioration across the multiseriate cellular structure of the timber was pronounced and cell erosion became apparent.

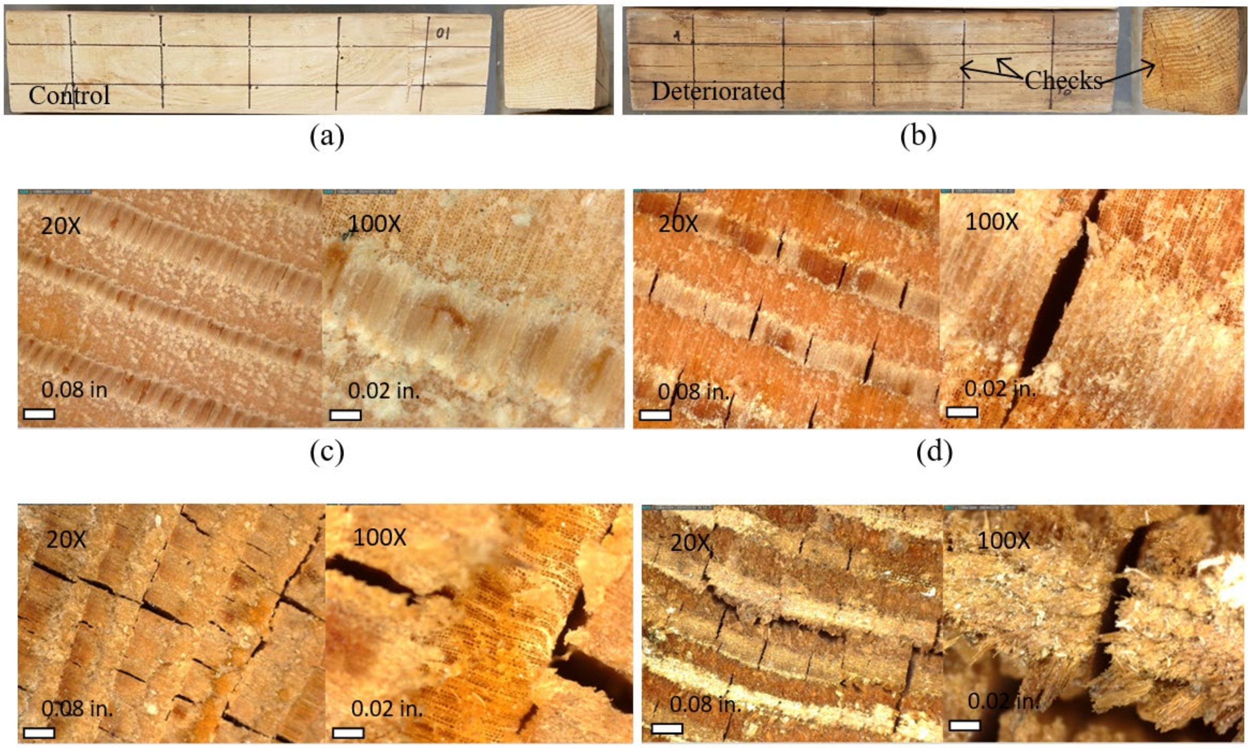

(a) (b)

(c) (d)

(e) (f)

Fig. I.2. Qualitative assessment on conditioning effects: (a) macroscopic view of control specimen; (b) macroscopic view of deteriorated specimen after three cycles; (c) microscopic views of control specimens; (d) microscopic views of specimens after one cycle; (e) microscopic views of specimens after three cycles; (f) microscopic views of specimens after six cycles

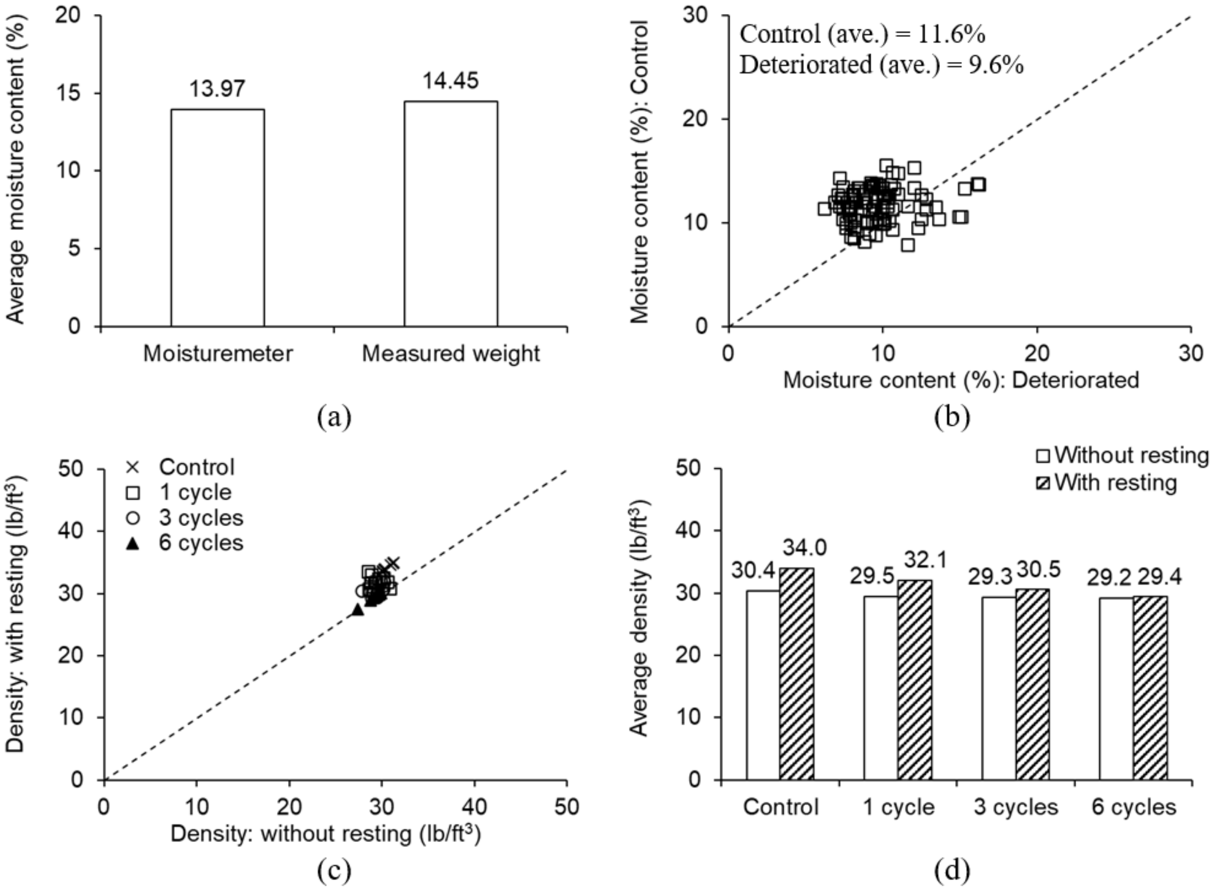

Fig. I.3. Moisture meter: (a) moisture meter reading vs. measured weight; (b) moisture content after one cycle; (c) density with and without resting; (d) average density

I.3.2. Moisture contents

Figure I.3(a) verifies the readings of the moisture meter against the measured weight of moisture. In light of equilibrium moisture contents on site, the specimens soaked for six weeks were taken out of the water tank and placed in the laboratory for one week at room temperature; afterward, their moisture contents were obtained. The mean values from the moisture meter and the scale agreed with a margin of 3.3% and were within the archetypal range of 10% to 15% for kiln-dried structural lumber (Shirmohammadi et al. 2021). The moisture contents of the control and deteriorated specimens are compared in Fig. I.3(b). The data of the specimens exposed to three and six cycles were not included since the succeeding oven-drying phases of ASTM D1037 (ASTM 2020) lowered the amount of moisture below the sensible range of the device (less than 6%). With regard to the primary purpose of the test (i.e., use of the nondestructive test devices for monitoring the condition of structural timber), the moisture of those specimens was not weighed. The moisture contents of the specimens were not higher than the fiber saturation point of Dougals Fir (typically, 30%, Bora et al. 2021), beyond which no more water uptake is available because micropores are fully filled. The transport of moisture was accomplished through a diffusion process in the cell walls and lumens of the species (Nguyen et al. 2021) and the reduced content of the deteriorated specimens was attributable to the malfunctioning of failed ray cells that carried fluids (Smallman and Bishop 1999), accompanied by increased friction forces in the cell structure (Jaskowska-Lemanska and Przesmycka 2021).

The 48-hour resting tended to elevate the density of the conditioned specimens (Fig. I.3(c)). The absorbed moisture may induce geometric instability in the deteriorated timber, driven by the anisotropic expansion of the cell walls (Carll and Wiedenhoeft 2009; Shirmohammadi et al. 2021). Shown in Fig. I.3(d) is the average density of the timber with and without resting (the control category with and without resting means the densities of the specimens in their as-is and oven-dried states, respectively). The decreased density of the specimens with the conditioning cycle implies the collapse of wood cells (Cabral et al. 2022) with enlarged lumen volumes (USDA. 1999; Via et al. 2003), aligning with the microscopic images portrayed in Fig. I.2. In addition, literature as to scanning electron microscopy (SEM) confirms that deteriorated wood contains expanded cavities alongside inferior crystallinity (Guo et al. 2018). Although density is a useful metric that represents the degradation of mechanical properties (Bandara et al. 2023), it cannot ascertain specific locations of damage. The variation of the densities points out that the initial mechanical properties of the timber would not be retained (Jaskowska-Lemanska and Przesmycka 2021).

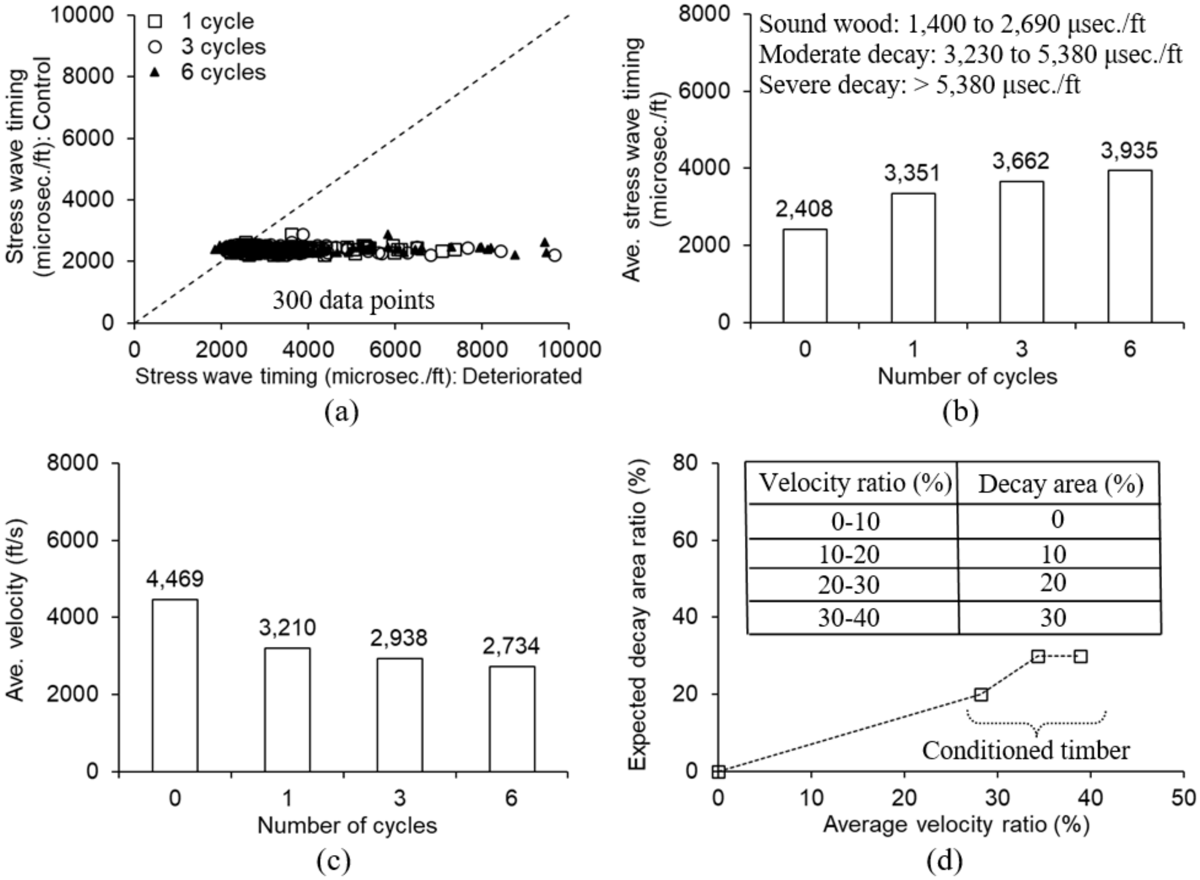

Fig. I.4. Stress wave timer: (a) measured wave timing; (b) average wave timing; (c) average velocity ratio; (d) expected decay area ratio

I.3.3. Stress wave timing

Figure I.4(a) plots the stress wave timing of the control and deteriorated specimens. The elapsed time of the conditioned ones parallel to the abscissa manifests the progression of internal damage. For clarity, the average stress wave timing of the individual categories was calculated and is provided in Fig. I.4(b). The transmission time of 2,408 microsec./ft belonging to the control category was within the range of the *Sound wood* category (1,400 to 2,690 microsec./ft, Brashaw et al. 2014), whereas the stress wave time gradually rose with the conditioning cycle and all values ranging from 3,351 to 3,935 microsec./ft were within the *Moderate decay* category (3,230 to 5,380 microsec./ft, Brashaw et al. 2014). Contrary to the coefficient of variation of the control specimens being COV = 0.039, those of the conditioned ones remarkably increased (COV = 0.345, 0.403, and 0.487 for the one-, three-, and six-cycled specimens, respectively) owing to the nondeterministic nature of deterioration. The travel velocity of the stress waves is charted in Fig. I.4(c), where the adequacy of the test method is reaffirmed since the average velocity of 4,469 ft/s for the control specimens fell within the range of 3,940 ft/s to 4,920 ft/s seen in undamaged timber (Kasal et al. 2010). The retarded velocities of the conditioned specimens are ascribed to the irregularly crushed cellular structure of the timber (Carreon and Carrillo 2021), which diminishes physical contacts necessary for transmitting wave signals. Figure I.4(d) infers decay areas in the test specimens based on a velocity ratio (V_R)

$$V_R(\%) = \frac{\left(V_{cont} - V_{\det}\right)}{V_{cont}} \times 100 \tag{I.1}$$

where V_{cont} and V_{det} are the velocities of the control (0 cycles) and deteriorated specimens (1 to 6 cycles), respectively. According to the inset of Fig. I.4(d) showing a rough estimation of decay areas (Dackermann et al. 2014), the conditioned timber was expected to have a decay area ratio spanning from 20% to 30% (Fig. I.4(d)). In view of the fact that timber elements are rated as deteriorated if a decay level is greater than 10% per the AASHTO inspection manual (AASHTO 2019), the accelerated test protocol of ASTM D1037 (ASTM 2020) appears to be acceptable in terms of reproducing the deterioration of in-situ timber bridges.

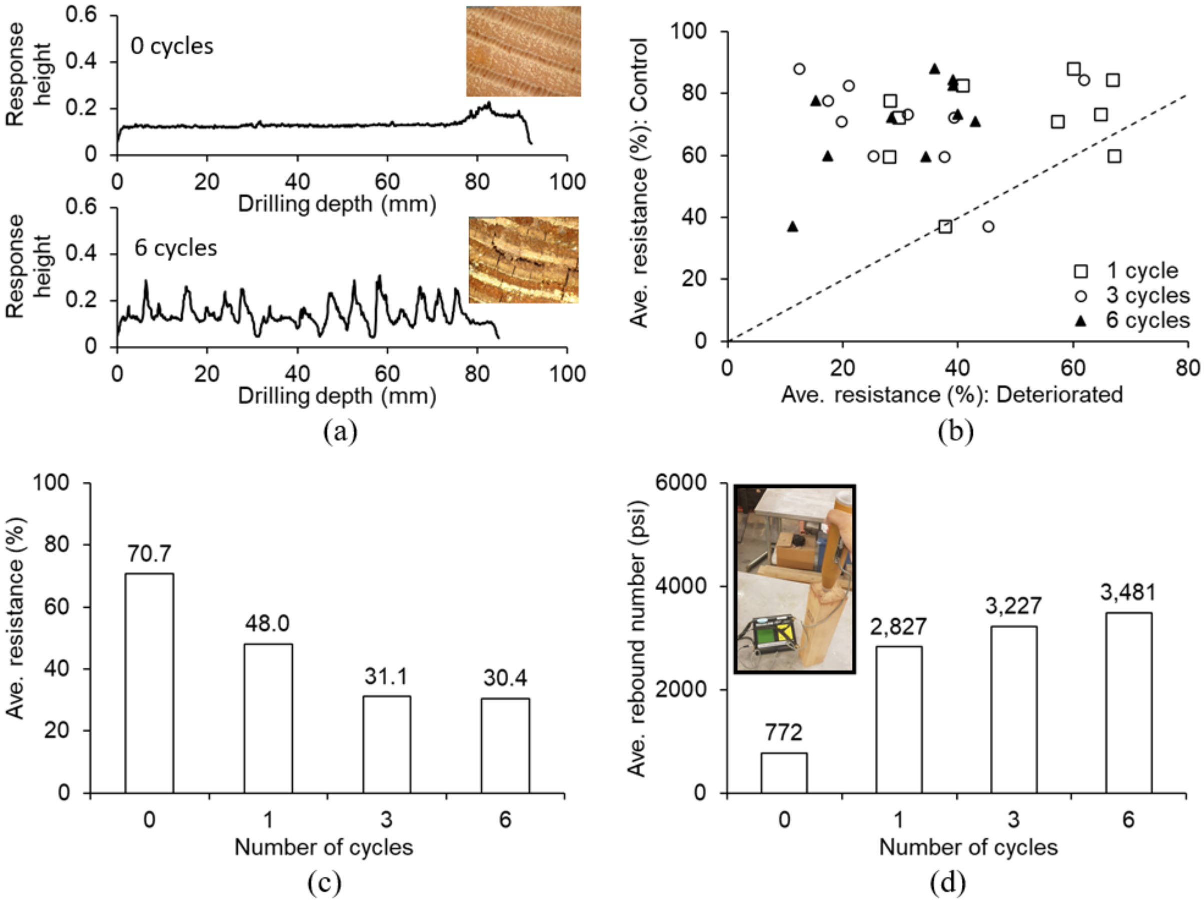

Fig. I.5. Microdrill: (a) individual data; (b) measured resistance; (c) average resistance; (d) rebound hammering

I.3.4. Microdrill

Microdrilling responses for the control and deteriorated specimens are given in Fig. I.5(a). If voids or discontinuities are inherent in the timber, drilling resistance would drop significantly. The consistent resistance of drilling at 0 cycles signifies that the control specimen had uniform quality across the cross section without physical decay pockets (Fig. I.5(a), up). By contrast, the fluctuating pattern of the deteriorated specimen at 6 cycles insinuates that the conditioning created nonhomogeneous configurations inside the timber (Fig. I.5(a), down); specifically, the periodic spikes of the resistance are related to the conformational arrangement of the grain constituents: hardened cell walls and collapsed lumens (Xu et al. 2013; Aloisio et al. 2023). The average resistance of the deteriorated specimens is contrasted with that of the control in Fig. I.5(b). The variability in the conditioned timber's responses resulted in disorganized data; nonetheless, the control category showed more resistance relative to the conditioned groups on most occasions. This inclination is underscored in Fig. I.5(c), instantiating the average ratios between peak and valley resistances. After one cycle of accelerated aging, there was a 32.1% reduction in the average resistance; however, the resistance level was preserved in the 3- and 6-cycled specimens. Fibers and vessels in the arranged cellular structure contributed to the internal stability of the wood during the drilling process (Hoadley 2000). Figure I.5(d) depicts the near-surface hardness of the specimens, represented by the readings of the rebound hammer. Hardening was obvious with the increased conditioning cycles due to the enhanced stiffness of the cell walls from lignin and the mechano-sorptive creep deformations of the fibers (Tarvainen et al. 2006; Xin et al. 2022). Additionally, the irreversible swelling of the surface layers was another influencing factor (Rautkari 2012).

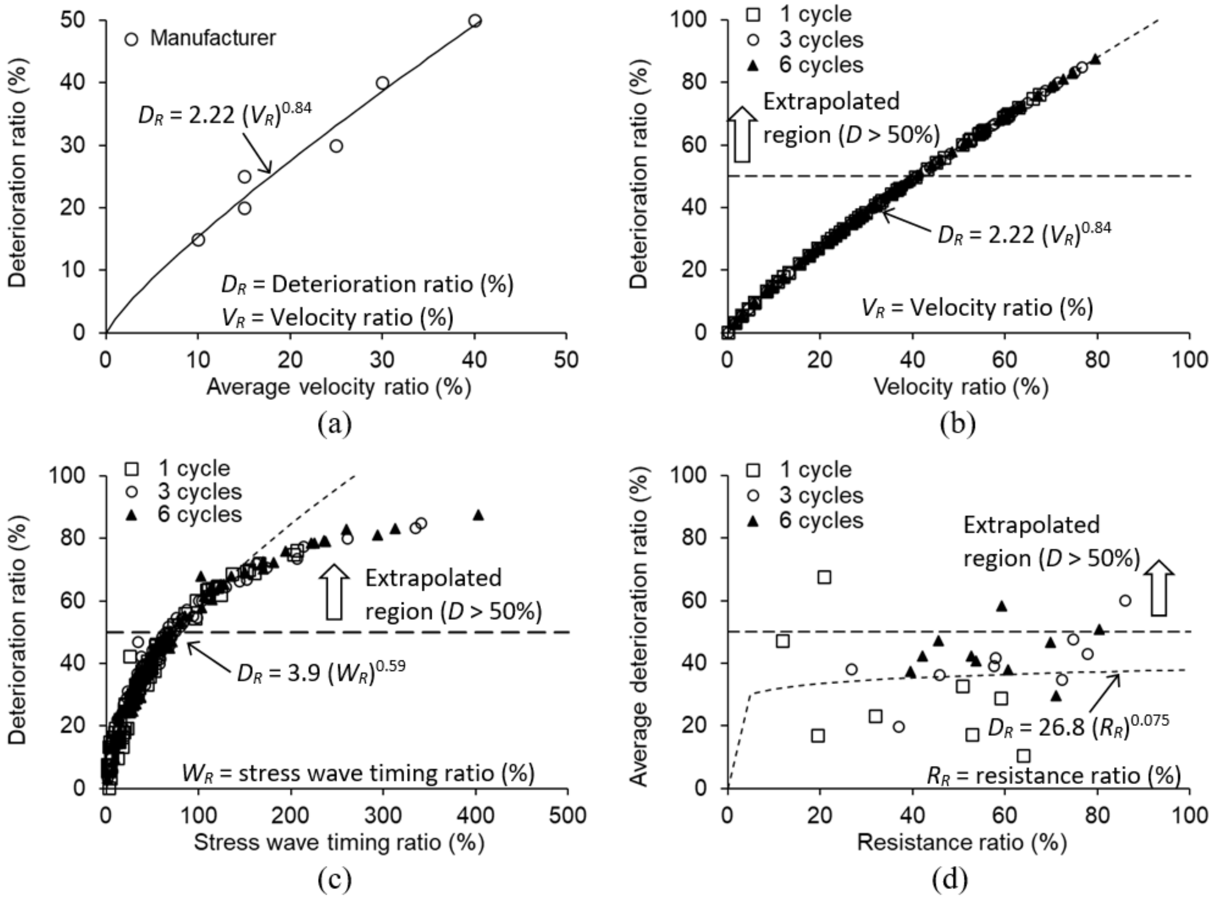

Fig. I.6. Determination of deterioration ratio: (a) calibration; (b) velocity ratio; (c) stress wave timing ratio; (d) resistance ratio

I.3.5. Quantitative deterioration

Coupled with the above-described nondestructive test results, the deterioration ratio of the specimens (D_R) that signifies a damage level is displayed in Fig. I.6 (D_R = 0%: intact and D_R > 0%: impaired). The manufacturer-supplied data were first fitted to build an equation (Fig. I.6(a)), mapping the domain of the velocity ratios (V_R, Eq. I.1) to the codomain of the deterioration ratios (D_R)

$$D_R = 2.22(V_R)^{0.84} \tag{I.2}$$

Next, Eq. I.2 was conjoined with the velocity ratios of the one- to six-cycled specimens (Fig. I.6(b)), which is necessary to interconnect output values from the nondestructive test methods; in other words, the velocity ratio, stress wave timing, and drilling resistance of a single test specimen are correlated and hence they can be converted to one another for predicting the degree of deterioration. Figure I.6(b) demonstrates that the regression equation is usable regardless of the conditioning cycles; nonetheless, even if the equation can generate a deterioration ratio greater than D_R = 50%, practitioners should be cautious in handling the extrapolated region of D_R > 50%. A relationship between the deterioration ratio (D_R) and the wave timing ratio (W_R, Eq. I.3) is shown in Fig. I.6(c) and their one-to-one correspondence was fitted (Eq. I.4):

$$W_R(\%) = \frac{(W_{\text{det}} - W_{cont})}{W_{cont}} \times 100 \tag{I.3}$$

$$D_R = 3.9(W_R)^{0.59} \tag{I.4}$$

where W_{det} and W_{cont} are the stress wave timing of the deteriorated and control specimens, respectively. Equation 4 matched the data pairs up to W_R = 125%, which was higher than the threshold value of W_R = 75.5% at the interpolated region limit of D_R = 50% (Fig. I.6(c)). As in the case of Eq. I.2, care should be exercised when dealing with W_R > 75.5%. For the implementation of Eq. I.3 on site, the average stress wave timing of W_{cont} = 2,408 microsec./ft may be taken as the baseline time (Fig. I.4(b)). Similarly, a resistance ratio from the microdrilling test (R_R, Eq. I.5) was employed to predict the level of deterioration (Fig. I.6(d) and Eq. I.6)

$$R_R\left(\%\right)=\frac{\left(R_{cont}-R_{\mathrm{det}}\right)}{R_{cont}}\times 100 \tag{I.5}$$

$$D_R=26.8\left(R_R\right)^{0.075} \tag{I.6}$$

where R_{cont} and R_{det} are the drilling resistance of the control and deteriorated specimens, respectively. The baseline resistance may be the average of the control specimen (R_{cont} = 70.7%, Fig. I.5(c)). As opposed to others (Figs. I.6(b) and (c)), the degree of dispersion was conspicuously high with the microdrilling method (Fig. I.6(d)). On that account, the velocity and stress wave ratios (V_R and W_R, respectively) should take precedence when determining a deterioration ratio (D_R), even though the resistance ratio (R_R) remains a viable means.

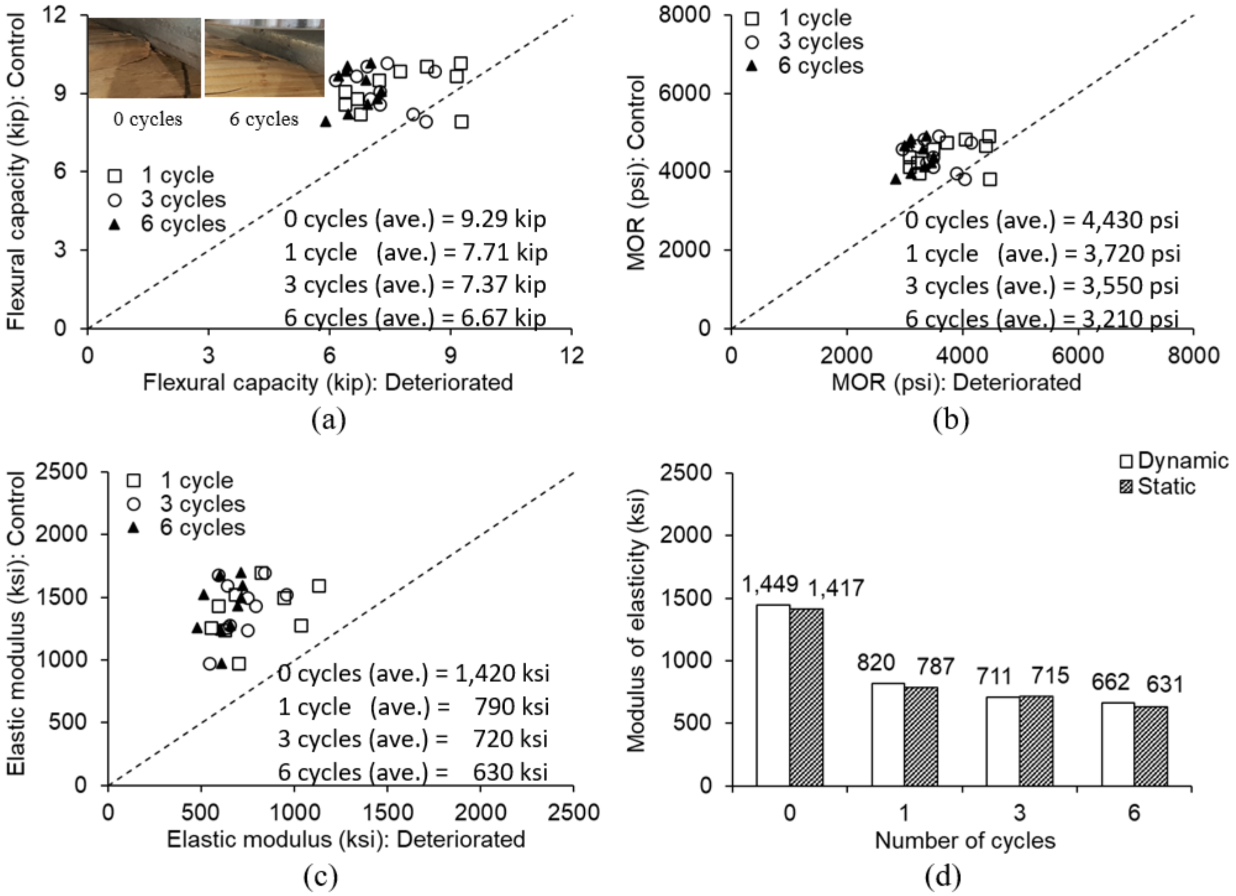

(a) (b)

(c) (d)

Fig. I.7. Three-point bending test: (a) flexural capacity; (b) modulus of rupture; (c) static elastic modulus; (d) comparison of average static and dynamic elastic moduli

I.3.6. Flexural response

The mechanical response of the specimens under destructive testing is rendered in Fig. I.7. The average flexural capacity of 9.29 kip for the control specimens noticeably abated with the increased cycles (Fig. I.7(a)), involving a drop of 16.1%, 20.0%, and 27.6% for those subjected to one, three, and six cycles, respectively. Likewise, the average modulus of rupture was lessened (Fig. I.7(b)). These downgraded strength-related properties are concerned with the previously-explained morphological changes in the cellulose and hemicellulose contents (Xin et al. 2022). As instructed in Fig. I.7(c), the accelerated aging provoked a decline in the elastic modulus of the specimens. The remarkable diminution of 44.4% from the control to the one-cycle-conditioned specimens (1,420 ksi and 790 ksi, respectively, on average) can be accounted for by the failure modes photographed in the inset of Fig. I.7(a): in contrast to the undamaged specimen exhibiting sharply fractured wood layers, the deteriorated specimen revealed indented compression fibers that brought about the softening of the timber. It is worth noting that the elastic moduli of all specimens were acquired within the initial linear-response stage of the flexural behavior, while the failure modes were adopted to articulate the fundamental source of the waned features. Figure 7(d) compares the dynamic (E_{dyn}, Eq. I.7) and static (structural analysis based on three-point bending) moduli of elasticity

$$E_{dyn} = \rho V^2 \tag{I.7}$$

where ρ is the density and V is the velocity of the stress wave (Ilharco et al. 2015). Irrespective of the conditioning cycles, the dynamic elastic modulus tended to be higher than their static counterparts because the local-level properties (dynamic) pertaining to the stress waves were influenced by the internal friction of the cell structures (Ross et al. 1999).

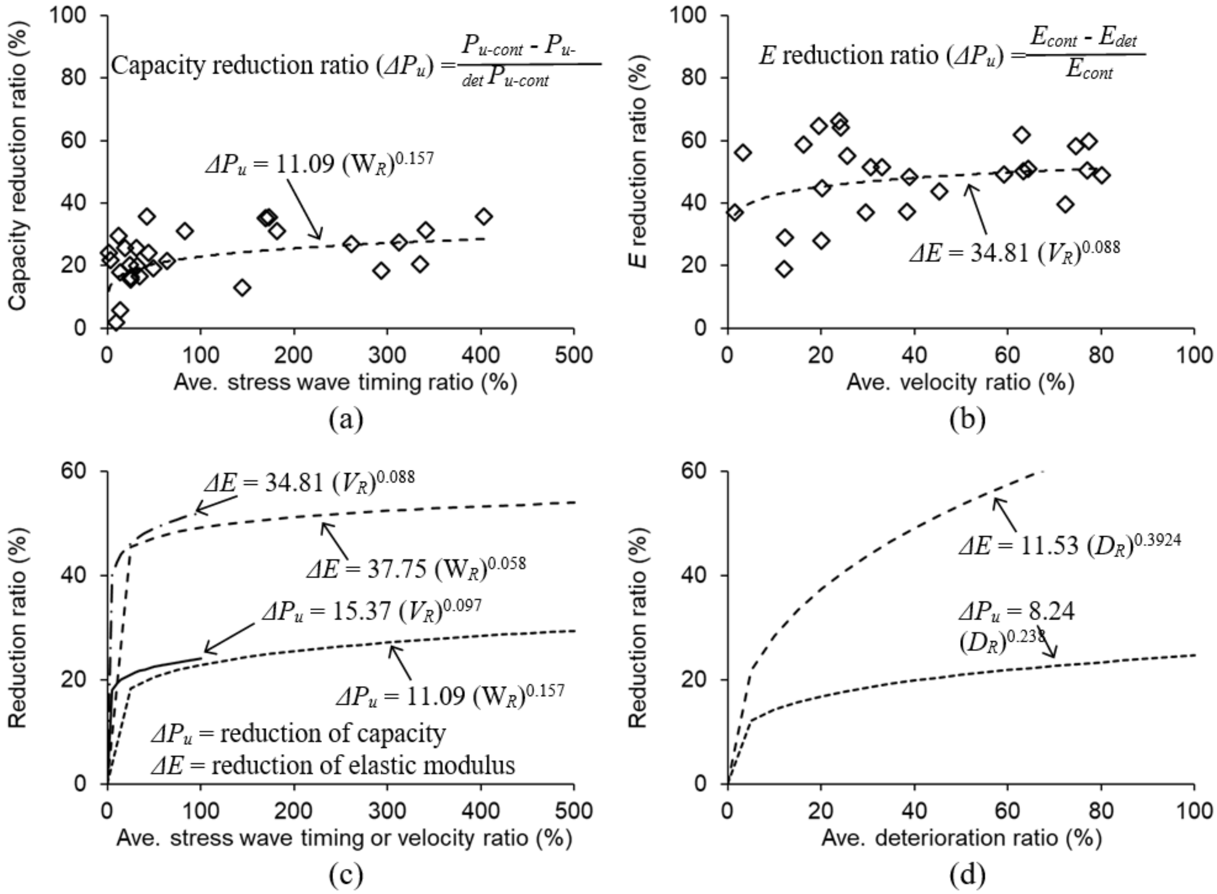

Fig. I.8. Relationship between non-destructive and destructive test results: (a) capacity reduction ratio with average stress wave timing ratio; (b) elastic modulus reduction ratio with average velocity ratio; (c) comparison between capacity and elastic modulus reduction ratios; (d) deterioration ratio

I.3.7. Link between destructive and nondestructive tests

Figure I.8 graphs mutual reliance between the destructive (ordinate) and nondestructive (abscissa) tests. The purpose of disclosing regression equations in Fig. I.8 is to impart a certain interaction trend between selected parameters rather than to provide absolute prediction metrics. When the stress timing ratio increased (W_R), the capacity reduction ratio of the specimens (ΔP_u) rapidly went up and stabilized in an asymptotic manner (Fig. I.8(a)). An analogous tendency was found in Fig. I.8(b) where the elastic modulus reduction ratio (ΔE) and the average velocity ratio (V_R) were associated. The amplified scatter of the ΔE vs. V_R response against that of the ΔP_u vs. W_R response was due to the sensitivity of the potentiometer that logged the displacement of the specimens. Contingent upon the evolution of the stress wave timing and velocity ratios, a comprehensive evaluation on the capacity and elastic modulus reduction ratios is made in Fig.

I.8(c). The slope of the V_R-related terms was stiffer than the slope of the W_R-related terms up to $\Delta P_u = 18\%$ and $\Delta E = 25\%$. Regarding the development of the reduction ratios, the elastic modulus expression (ΔE) was more reactive in comparison with the capacity expression (ΔP_u). These observations corroborate that the outcomes of the stress wave timer can better be utilized for detecting a change in the elastic modulus of the deteriorated timber over the flexural capacity. Figure I.8(d) shows the dependency of the reduction ratios on the deterioration ratio (D_R). The large discrepancy between ΔE and ΔP_u denotes that the deterioration of the specimens almost linearly affected the degradation of their elastic modulus; contrarily, the correlation between the deterioration ratio and the capacity reduction ratio was relatively insignificant. Hence, in a practical sense, the succeeding hypothesis is put forward: the deterioration of timber dominates the serviceability limit state of structures concerning the modulus of elasticity, whereas it would have a limited impact on their ultimate limit state.

I.4. Recommendations

Experimental results are integrated with machine learning technologies to propose practice guidelines. As enumerated in Table I.2, all test categories are statistically significant and will be relevant in formulating methodological criteria. After completing required procedures, validated computational models are used for comprehending the degree of deterioration with respect to nondestructive test parameters (Fig. I.9(a)). Recommendations are made to assist practitioners in decision-making.

Table I.2. Analysis of variance (ANOVA)

Parameter	Sum of squares	Degrees of freedom[a]	Mean square	F_0	*P* value	$F_{critical}$	Significance
Moisture content	690.1	198	3.49	58.82	7.6E10^{-13}	3.89	Significant
Density (dry)	4,916.8	36	136.57	5.48	0.0033	2.87	Significant
Density (wet)	5,527.6	36	153.5	66.71	8.9E10^{-15}	2.87	Significant
Stress wave timing	536,135	396	1,353.9	24.59	1.3E10^{-14}	2.63	Significant
Velocity	28E10^{6}	396	69,743	45.42	3.0E10^{-25}	2.63	Significant
Microdrill resistance	7,851.0	36	218.1	16.43	6.8E10^{-7}	2.87	Significant
Rebound	206.6	36	5.74	125.85	3.9E10^{-19}	2.87	Significant

[a]: within groups

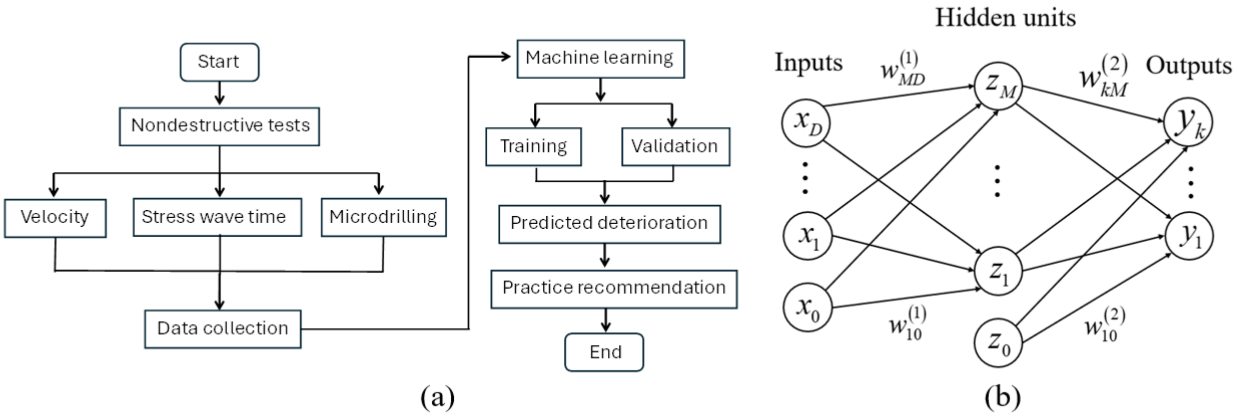

Fig. I.9. Computational modeling: (a) flowchart; (b) three-layer neural network model (reproduced from Bishop and Bishop 2024)

I.4.1. Machine learning

Two machine learning algorithms were applied to predict the response of the deteriorated specimens: neural networks and polynomial regression. A concise description is provided here, with further details available elsewhere (Chopra and Khurana 2023; Bishop and Bishop 2024). The neural network model, inspired by the function of the human brain, was constituted with input, hidden, and output layers with interconnected artificial neurons that processed information (Fig. I.9(b)). The networks were able to handle highly nonlinear and unstructured data (Ghosh and Ghosh 2024). Predictions from the three-layer network model were governed by (Bishop and Bishop 2024)

$$y_k\left(\mathbf{x},\mathbf{w}\right)=f\left(\sum_{j=0}^{M}w_{kj}^{(2)}h\left(\sum_{i=0}^{D}w_{ji}^{(1)}x_i\right)\right) \tag{I.8}$$

where $y_k(\mathbf{x},\mathbf{w})$ is the output of the k^{th} neuron; **x** and **w** are the input and weight vectors, respectively; f(.) is the output-unit activation function; h(.) is the differentiable activation function; M is the number of the hidden neurons; D is the number of the input features; and x_i is the i^{th} feature of the input vector. Hyperparameter-tuning was implemented with the grid search method to appropriately identify the number of the hidden layers (Owen 2022). To assure the predicted response of the neural network algorithm, an intuitive polynomial regression algorithm was executed. The high-order terms of the regression technique were expressed as (Chopra and Khurana 2023)

$$y = \theta_0 + \sum_{i=1}^{m} \theta_i X^m \qquad \text{(I.9)}$$

where y is the predicted response; θ_i is the coefficient of the i^{th} term; m is the number of the polynomial order; and X is the regressor.

The experimental data set was randomly divided into 80% for training and 20% for validation, which are archetypal ratios in machine learning (Prosise 2022). Then, the algorithms were deployed and the degree of accuracy was monitored by calculating the mean absolute error (MAE, Eq. I.10) and the coefficient of determination (R^2, Eq. I.11) until convergence was achieved

$$MSE = \frac{1}{n} \sum_{i=1}^{n} \left(y_i - y_p \right)^2 \qquad \text{(I.10)}$$

$$R^2 = 1 - \frac{\sum_{i=1}^{n} \left(y_i - y_p \right)^2}{\sum_{i=1}^{n} \left(y_i - \bar{y} \right)^2} \qquad \text{(I.11)}$$

where n is the number of the data points; y_i and y_p are the target and predicted values, respectively; and $\bar{y}$ is the sample mean. From a mathematical standpoint, the accuracy of the model predictions is improved with low MSE and high R^2 values.

Figure I.10 arrays the training and validation stages of the machine learning algorithms. The polynomial regression (Figs. I.10(a) and (b)) and neural network (Figs. I.10(d) and (e)) approaches were satisfactory with the coefficients of determination of R^2 = 0.9399 to 0.9999 for the velocity and stress wave timing ratios (Table I.3); however, disparities were noticed in the drilling resistance ratios (Fig. I.10(c) and (f)) owing to the large scatter of the test data (Fig. I.6(d)). Discussions continue in the next sections.

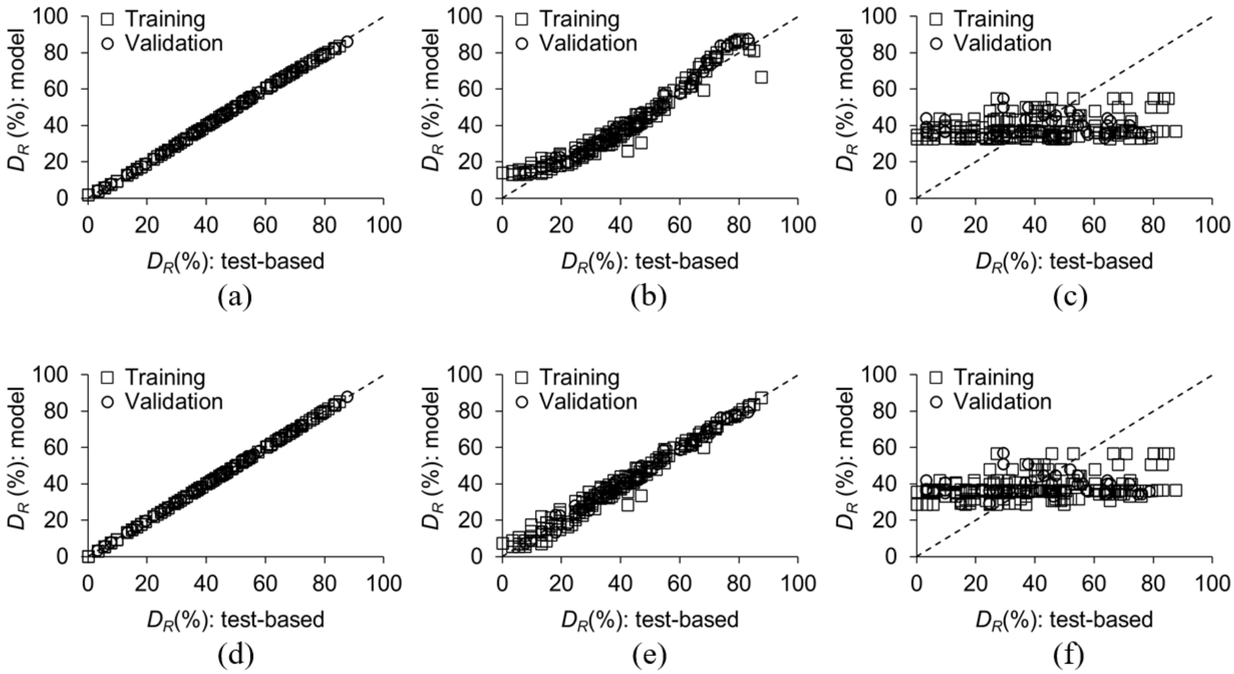

Fig. I.10. Training and validation for predicting deterioration ratio: (a) polynomial regression with velocity ratio; (b) polynomial regression with stress wave timing ratio; (c) polynomial regression with drilling resistance ratio; (d) neural network with velocity ratio; (e) neural network with stress wave timing ratio; (f) neural network with drilling resistance ratio

Table I.3. Appraisal of machine learning algorithms

Method		Training			Validation		
		V_R	W_R	R_R	V_R	W_R	R_R
PR	MAE	0.2586	3.1173	18.4141	0.2652	2.5743	13.5408
	R^2	0.9995	0.9399	0.0791	0.9995	0.9536	0.4713
NN	MAE	0.3397	4.0541	17.0164	0.3550	3.2897	17.7156
	R^2	0.9999	0.9768	0.0524	0.9999	0.9833	0.5938

PP = polynomial regression; NN = neural network; V_R = velocity ratio; W_R = stress wave timing ratio; R_R = drilling resistance ratio; MAE = mean absolute error; R^2 = coefficient of determination

I.4.2. Parametric studies

To understand the implications of varying nondestructive test ratios (V_R, W_R, and R_R) for the deterioration ratio (D_R) of Douglas Fir, the verified machine learning algorithms were extended for computational parametric studies. The variation of the input ratios was set to the feasible range of the experimental data ($0\% \leq V_R \leq 39\%$, $0\% \leq W_R \leq 63\%$, and $0\% \leq R_R \leq 57\%$). Figure I.11(a) shows the convergence of the polynomial regression method paired with randomly selected samples within the prescribed boundaries of all input data. The average deterioration ratio leveled off after 100 epochs; in consequence, 10,000 epochs were conservatively chosen for the parametric investigations. The sensitivity of the baseline ratios for V_R, W_R, and R_R is visualized in Figs. I.11(b) to (d) with a deviation range of ±15%, reflecting uncertainties in on-site timber. As the baseline velocity was increased, the deterioration ratios ascended up to 58.3% at a velocity of $V = 2{,}630$ ft/s (Fig. I.11(b)) with good agreement between the two machine learning approaches. The repercussions of adjusting the baseline stress wave timing are given in Fig. I.11(c), demonstrating an opposite propensity relative to the velocity case. The sensitivity of the baseline drilling resistance was generally inappreciable within the experimental boundary of 30% and 50% (Fig. I.11(d)), confirming that the drilling resistance ratio was not a primary factor in estimating the deterioration of structural timber (it still remains beneficial for detecting local flaws, though).

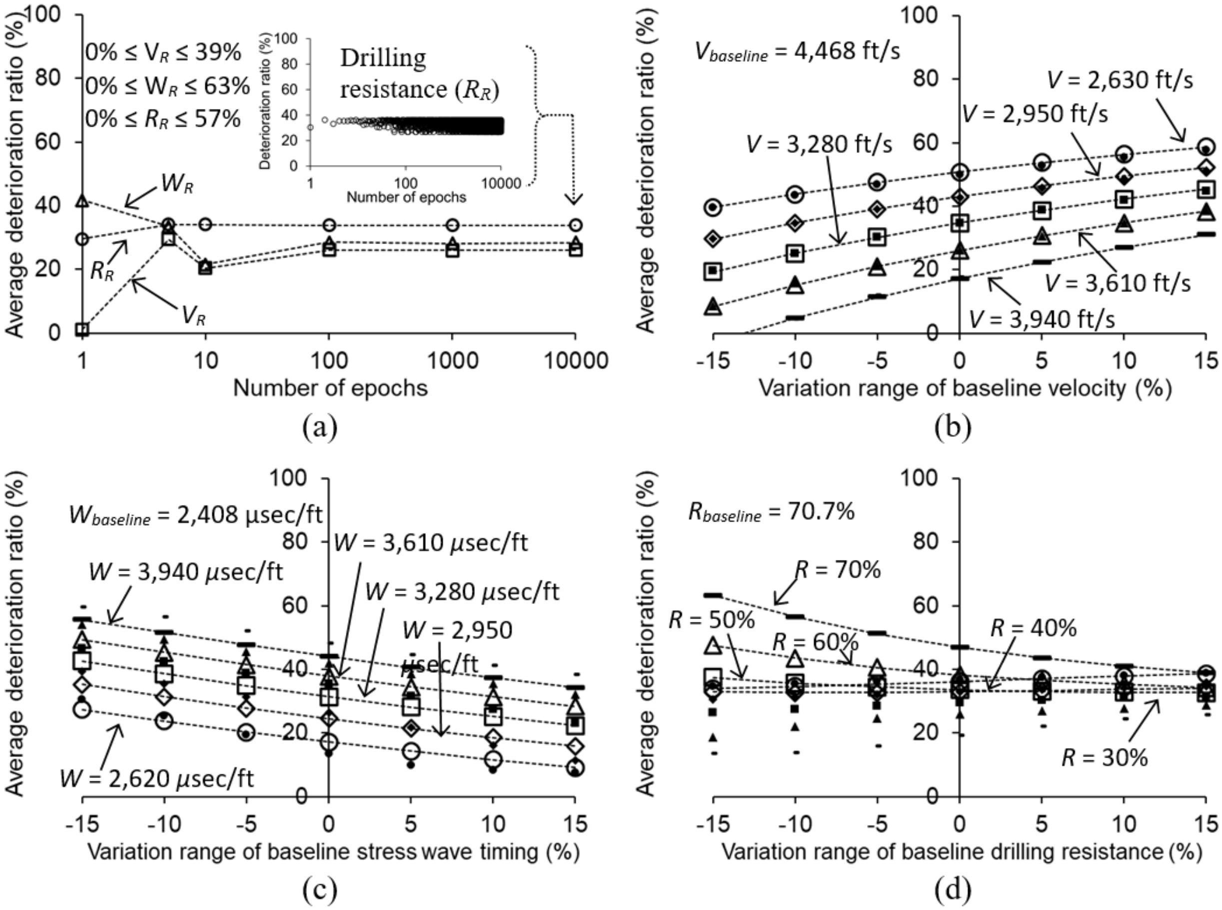

Fig. I.11. Sensitivity analysis (hollow: polynomial regression; solid: neural network): (a) random data sampling; (b) velocity ratio; (c) stress wave timing ratio; (d) drilling resistance ratio

I.4.3. Performance classification

In compliance with the present test results and published literature (Brashaw et al. 2014; Dackermann et al. 2014), the diverse values of the velocity, stress wave timing, and drilling resistance ratios were entered to categorize three condition states (Good, Moderate, and Fair in Table I.4). The velocity ratios of V_R = 0% to 30% encompassed a decay area of up to 20% (Fig. I.4(d)), while the stress wave timing ratios of W_R = 12%, 34%, and 123% were attained from the stress wave magnitudes of 2,690 microsec./ft, 3,230 microsec./ft, and 5,380 microsec./ft (Fig. I.4(b)), respectively. The upper drilling resistance ratio of 48% covered all deteriorated specimens (Fig. I.5(c)). These sampling cohorts enabled stochastic simulations using the machine learning algorithms (Fig. I.12(a)) and the computed mean values are described in Fig. I.12(b). For practicality, Table I.4 lists rounded deterioration ratios for the three condition states.

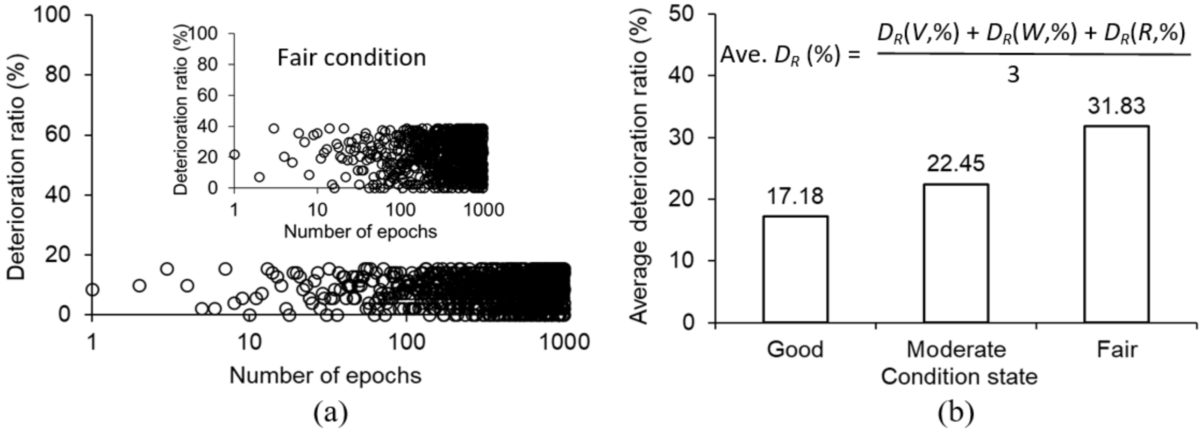

Fig. I.12. Practice recommendations: (a) random simulation using velocity ratios regression under Good condition; (b) average deterioration ratio

Table I.4. Proposed practice recommendations

Parameter	Condition state		
	Good	Moderate	Fair
Velocity ratio*	0% ≤ V_R ≤ 10%	0% ≤ V_R ≤ 20%	0% ≤ V_R ≤ 30%
Stress wave timing ratio*	0% ≤ W_R ≤ 12%	0% ≤ W_R ≤ 34%	0% ≤ W_R ≤ 123%
Drilling resistance ratio*	0% ≤ R_R ≤ 48%	0% ≤ R_R ≤ 48%	0% ≤ R_R ≤ 48%
Deterioration ratio (D_R)	15%	20%	30%

*: Random sampling ranges

I.5. Summary and Conclusions

This report has dealt with an experimental program in regard to deterioration mechanisms and ensuing consequences for structural timber, Douglas Fir. Conforming to ASTM D1037 (ASTM 2020), specimens were exposed to a series of soaking, steaming, freezing, and oven-drying cycles. Changes in the properties of the deteriorated timber were quantified by nondestructive methods (i.e., moisture metering, stress wave timing, and microdrilling). Supplementary tests such as rebound hammering and digital microscopy were conducted to elucidate the influence of the aggressive environmental exposure at the surface and near-surface levels. The conditioned specimens were loaded in three-point bending until failure, and their elastic modulus and load-resisting capacities were recorded. The nondestructive and destructive test results were then evaluated comparatively. For computational examinations, machine learning algorithms were employed and the trained/validated models produced data that were essential for developing performance classifications. The following are concluded:

- The accelerated conditioning of Douglas Fir altered its surface color from light brown to reddish brown, entailing anisotropic damage with multiple longitudinal checks. Besides, moisture absorption resulted in local swelling and elevated splitting stresses. The irregular deterioration of the multiseriate cellular structure prompted cell erosion.
- The moisture contents of all specimens were consistently lower than a fiber saturation point of 30%. In the decayed wood, enlarged voids and reduced crystalline integrity were palpable with a decrease in density.
- As the internal damage of the specimens intensified, the stress wave timing escalated from 2,408 microsec./ft to 3,936 microsec./ft. The nondeterministic attribution of deterioration scaled up the degree of scatter. By the same token, the average travel velocities across the specimens slowed from 4,467 ft/s to 2,735 ft/s. As far as microdrilling is concerned, stable resistance profiles evolved toward those incorporating periodic peaks with degradation characterized by hardened cell walls and collapsed lumens.
- Regression equations were calibrated to predict the deterioration ratio (D_R) of the conditioned timber on the basis of the velocity, stress wave timing, and drilling resistance

ratios (V_R, W_R, and R_R, respectively). Allowing for the manufacturer-provided application range, caution is advised when $D_R > 50\%$ is computed.

- On the destructive test, a reduction in the flexural capacity and elastic modulus of the aged timber was obvious by up to 27.6% and 55.5%, respectively. The response ratios of the capacity and modulus soared as the stress wave timing and velocity ratio increased, while the reactivity of the modulus term was more prominent than that of the capacity term.
- Sensitivity analysis clarified that the deterioration ratios reacted with the baseline velocity and stress wave timing ratios; on the contrary, the contribution of the baseline drilling resistance was marginal.
- Three condition states (Good, Moderate, and Fair) were proposed within the boundaries of $0\% \leq V_R \leq 30\%$, $0\% \leq W_R \leq 123\%$, and $0\% \leq R_R \leq 48\%$. The machine learning algorithms suggested the deterioration ratios from $D_R = 15\%$ to 30% for impaired structural members constructed with Douglas Fir.

I.6. References

AASHTO. 2019. Manual for bridge element inspection, American Association of State Highway and Transportation Officials, Washington, D.C.

Aloisio, A., Ussher, E., Fragiacomo, M., and Tomasi, R. 2023. Capacity models for timber under compression perpendicular to grain with screw reinforcement, European Journal of Wood and Wood Products, 81, 633-654.

ASTM. 2015. Standard test methods of static tests of lumber in structural sizes (ASTM D198-15), ASTM International, West Conshohocken, PA.

ASTM. 2020. Standard test methods for evaluating properties of wood-base fiber and particle panel materials (ASTM D1037-12), ASTM International, West Conshohocken, PA.

Baar, J., Paschova, Z., Cermak, P., and Wimmer, R. 2019. Color changes of various wood species in response to moisture, Wood and Fiber Science, 51(2), 1-13.

Bandara, S. Rajeev, P., and Gad, E. 2023. Structural health assessment techniques for in-service timber poles, Structure and Infrastructure Engineering, 19(4), 439-459.

Bishop, C. M. and Bishop, H. 2024. Deep learning: foundations and concepts, Springer, Cham, Switzerland.

Bora, S., Sinha, A., and Barbosa, A.R. 2021. Effect of wetting and redrying on performance of cross-laminated timber angle bracket connection, Journal of Structural Engineering, 147(9), 04021121.

Brashaw, B., Wacker, J., and Ross, R.J. 2014. Advanced timber bridge inspection, Duluth Natural Resources Research Institute, University of Minnesota Duluth, Duluth, MN.

Brashaw, B., Dahlberg, J., Hosteng, T., and Wacker, J. 2015. Development and integration of advanced timber bridge inspection techniques for NBIS, Report No. MN/RC2015-01, Natural Resources Research Institute, Duluth, MN.

Cabaleiro, M., Branco, J.M., Sousa, H.S., and Conde, B. 2018. First results on the combination of laser scanner and drilling resistance tests for the assessment of the geometrical condition of irregular cross-sections of timber beams, Materials and Structures, 51, 98-99.

Cabral, J.P., Kafle, B., Subhani, M., Reiner, J., and Ashraf, M. 2022. Densification of timber: a review on the process, material properties, and application, Journal of Wood Science, 68:20, s10086-022-02028-3.

Carll, C. and Wiedenhoeft, A.C. 2009. Moisture-related properties of wood and the effects of moisture on wood and wood Products. Moisture Control in Buildings: The Key Factor in Mold Prevention (2nd ed.), ASTM International, West Conshohocken, PA.

Carreon, H. and Carrillo, M. 2021. Determination of the ultrasonic velocity on a recent and aged pine wood, Proceedings of the 48th Annual Review of Progress in Quantitative Nondestructive Evaluation (QNDE2021), American Society of Mechanical Engineers, V001T21A001.

Chopra, D. and Khurana, R. 2023. Introduction to machine learning with Python, Bentham Books, Singapore.

Dackermann, U., Crews, K., Kasal, B., Li, J., Riggio, M., Rinn, F., and Tannert, T. 2014. In situ assessment of structural timber using stress-wave measurements, Materials and Structures, 47, 787-803.

Dahlberg, J., Phares, B., and Klaiber, W. 2015. Cost-effective timber bridge repairs: manual for repairs of timber bridges in Minnesota, Report No. MN/RC2015-45B, Minnesota Department of Transportation, St. Paul, MN.

Deng, X., Peng, W., Wu, X., Xiao, F., Ye, C., and Li, K. 2024. Effect of tracheid on water absorption behavior of Cunninghamia lanceolata under freeze-thaw conditions, European Journal of Wood and Wood Products, doi.org/10.1007/s00107-024-02099-7

Duquette, B.A. 2021. Evaluation of decay effect on tension perpendicular to grain properties of wood, MS Thesis, Mississippi State University, Starkville, MS.

Fosnacht, D. 2020. Development of cost-competitive timber bridge designs for long term performance, Final Report 2020-16, Natural Resources Research Institute, University of Minnesota Duluth, Duluth, MN.

Ghosh, P. and Ghosh, S. 2024. Neural network and neural computing, Intelligent Decision Making Through Bio-Inspired Optimization, IGI Global, Hershey, PA.

Guo, J., Zhou, H., Stevanic, J.S., Dong, M., Yu, M., Salmen, L., and Yin, Y. 2018. Effects of ageing on the cell wall and its hygroscopicity of wood in ancient timber construction, Wood Science and Technology, 52, 131-147.

Hoadley, R.B. 2000. Understanding wood, The Taunton Press, Newtown, CT.

Honfi, D., Lechner, T., and Kohler, J. 2017. Rational maintenance of timber bridges, 3rd International Conference on Timber Bridges, 10 pp.

Jaskowska-Lemanska, J. and Przesmycka, E. 2021. Semi-destructive and non-destructive tests of timber structure of various moisture contents, Materials, 14, 96, ma14010096.

Ilharco, T., Lechner, T., and Nowak, T. 2015. Assessment of timber floors by means of non-destructive testing methods, 101, 1206-1214.

Kacik, F., Smira, P., Kacikova, D., Reinprecht, L., and Nasswettrova, A. 2014. Chemical changes in fir wood from old buildings due to ageing, Cellulose Chemistry and Technology, 48(1-2), 79-88.

Kasal, B., Lear, G., and Tannert, T. 2010. Stress waves, In situ assessment of structural timber, RILEM state-of-the-art reports, Springer, Dordrecht, the Netherlands.

Kromoser, B., Spitzer, A., Ritt, M., and Grabner, M. 2024. Wooden bridges: strategies for design, construction and wood Species - from tradition to future, International Journal of Architectural Heritage, 18(4), 652-668.

Kumavat, H.R., Chandak, N.R., and Patil, I.T. 2021. Factors influencing the performance of rebound hammer used for non-destructive testing of concrete members: a review, Case Studies in Construction Materials, 14, e00491.

Nguyen, D.M., Almeida, G., Nguyen, T.M.L., Zhang, J., Lu, P., Colin, J., and Perre, P. 2021. A critical review of current imaging techniques to investigate water transfers in wood and biosourced materials, Transport in Porous Media, 137, 21-61.

Owen, L. 2022. Hyperparameter tuning with Python, Packt Publishing, Birmingham, UK.

Palma, P. and Steiger, R. 2020. Structural health monitoring of timber structures- review of available methods and case studies, Construction and Building Materials, 248, 118528.

Prosise, J. 2022. Applied machine learning and AI for engineers, O'Reilly Media, Sebastopol, CA.

Radford, D.W., Van Goethem, D., Gutkowski, R.M., and Peterson, M.L. 2002. Composite repair of timber structures, Construction and Building Materials, 16, 417-425.

Rashidi, M., Hoshyar, A.N., Smith, L., Samali, B., and Siddique, R. 2021. A comprehensive taxonomy for structure and material deficiencies, preventions and remedies of timber bridges, Journal of Building Engineering, 34, 101624.

Rautkari, L. 2012. Surface modification of solid wood using different techniques, Department of Forest Products Technology, Aalto University, Helsinki, Finland.

Ross, R.J., Pellerin, R.F., Volny, N., Salsig, W.W., and Falk, R.H. 1999. Inspection of timber bridges using stress wave timing nondestructive evaluation tools, General Technical Report: FPL-GTR-114, United States Department of Agriculture, Washington, D.C.

Shirmohammadi, M., Leggate, W., and Redman, A. 2021. Effects of moisture ingress and egress on the performance and service life of mass timber products in buildings: a review, Construction and Building Materials, 290, 123176.

SFI. 2023. Comparing SFI and FSC certification standards, Sustainable Forestry Initiative, Washington, D.C.

Smallman, R.E. and Bishop, R.J. 1999. Materials for sports, Modern Physical Metallurgy and Materials Engineering, 406-419.

Smith, I., Landis, E., and Gong, M. 2003. Fracture and fatigue in wood, John Wiley & Sons, West Sussex, UK.

Sundararaj, R. 2022. Science of wood degradatoin and its protection, Springer Nature, Singapore.

Tarvainen, V., Ranta-Maunus, A., Hanhijarvi, A., and Forsen, H. 2006. The effect of drying and storage conditions on case hardening of Scots pine and Norway spruce timber, Maderas, Ciencia y Tecnologia, 8(1), 3-14.

USDA. 1999. Wood handbook: wood as an engineering material. General Technical Report FPL-GTR-113. U.S. Department of Agriculture, Forest Service, Forest Products Laboratory, Madison, WI.

USDA. 2010. Wood handbook: wood as an engineering material (centennial edition), United States Department of Agriculture, Madison, WI.

Via, B.K., Shupe, T.F., Groom, L.H., Stine, M., and So, C.-L. 2003. Multivariate modeling of density, strength and stiffness from near infrared spectra for mature, juvenile and pith wood of longleaf pine (pinus palustris). Journal of Near Infrared Spectroscopy 11(5): 365-378.

Wang, H., Yuan, S., Zhang, J., and Li, Q. 2021. Influence of four ageing methods on the mechanical properties of bamboo scrimber, International Journal of Polymer Science, 2021, 2478525.

White, R.H. and Ross, R.J. 2014. Wood and timber condition assessment manual: second edition. General Technical Report FPL-GTR-234, U.S. Department of Agriculture, Madison, WI.

Xin, Z., Fu, R., Zong, Y., Ke, D., Zhang, H., Yu, Y., and Zhang, W. 2022. Effects of natural ageing on macroscopic physical and mechanical properties, chemical components and microscopic cell wall structure of ancient timber members, Construction and Building Materials, 359, 129476.

Xu, B.-H., Bouchair, A., Taazount, M., and Racher, P. 2013. Numerical simulation of embedding strength of glued laminated timber for dowel-type fasteners, Journal of Wood Science, 59, 17-23.

Yu, Y., Liu, Y., Gong, M., Xu, Z., and Fang, Y. 2017. R&R study of using a stress wave timer to measure the elastic modulus of structural dimension lumber, Measurement, 95, 293-296.

Part II: Nondestructive Testing for Condition Evaluation of Timber Bridges: Synthesis of Qualitative and Quantitative Methodologies by Machine Learning

II.1. Introduction

The sustainability of highway bridges is of global interest. As of 2023, there are 42,391 structurally deficient bridges in the United States (6.8% of 621,510 bridges) and more than $319 billion is needed to repair poor condition bridges (ARTBA 2023). Unlike other construction materials such as concrete and steel, wood is susceptible to deterioration stemming from aggressive environments, overloading, and organic decomposition (Reinprecht 2016). Timely evaluations and preservation activities are thus salient to maintain the quality and reliability of timber bridges. Despite the rigorous effort of inspection engineers, contemporary methodologies are largely empirical without measuring the properties and performance of existing bridges (Abdallah et al. 2021). Inaccurate evaluations require transportation authorities to allocate extra funds for dispensable tasks and overlook critical problems that necessitate appropriate repairs. Visual inspections are dominantly employed in the field to detect local splitting, staining, and checks (Rashidi et al. 2021); however, damage might remain unseen and internal decay could degrade the capacity of load-bearing members. For these reasons, conventional methods are insufficient to assess such bridge structures and precise information should be collected during site inspections so that adequate technical actions can follow.

A wide variety of techniques, including mechanical loadings and nondestructive tests, are available to estimate the condition state of timber bridges (Palma and Steiger 2020). From a practical standpoint, moisture metering, stress wave timing, and microdrilling are representative nondestructive test methods for timber bridges (Brashaw et al. 2014). Recognizing the importance of moisture as an attribute that controls the strength and durability of structural lumber (Palma and Steiger 2020), the content of internal moisture should be appropriately logged by a moisture meter during inspections. A moisture content of 20% may be regarded as the threshold limit (Rashidi et al. 2021); accordingly, in-situ bridges should have a content of less than the limit. A stress wave timer handles the transmission of acoustic signals across timber. A pair of accelerometers are mounted at designated positions and signals created from an exciter are received by the other transducer. Upon analyzing gathered signals, physical properties are gauged and suspected flaws are uncovered (Palma and Steiger 2020). A baseline transmission value is set to represent the sound condition of a bridge and elapsed timing is contrasted to predict the severity of degradation. Details on the principle and implementation of stress wave timers are referenced in ASTM D6874-21 (ASTM 2021). As far as microdrilling is concerned, an electrically powered needle-like bit penetrates timber and the mechanical torque of the bit imparts response information (White and Ross 2014). The presence of voids within the timber is determined by comparing resistance data from undamaged portions: a substantially dropped profile implies that the location has significant decay.

Notwithstanding the popularity of the aforementioned nondestructive test technologies, bridge evaluations are still dependent upon visual inspections as in the case of the National Bridge Inventory program of the Federal Highway Administration (FHWA 2014). The underlying rationale is ascribed to the lack of a specific link between the convenient (visual) and rigorous (instrumentation-focused) approaches. This paper seeks to reframe customary inspection and evaluation practices for timber bridges by incorporating nondestructive tests. To save developmental endeavors, commercially available devices have been adopted and their accuracy and applicability were previously appraised via laboratory testing (Kim and Ha 2024). The verified technologies are implemented in the current research to examine the condition of ten bridges and measured data are utilized for the assessment of visual inspection results. Afterward, recommendations are suggested to integrate these qualitative and quantitative methodologies with the aim of refining field rating strategies.

II.2. Research Significance

The construction of timber bridges was prevalent before the 1950's and many of them continue to be in service. Given that their usable service lives have already exceeded or are close to 75 years, which is mandated by the American Association of State Highway and Transportation Officials (AASHTO)) Load and Resistance Factor Design (LRFD) Bridge Design Specifications (AASHTO 2020), properly diagnosed condition states are deemed crucial. However, a high level of variability and uncertainty in wood make structural evaluation difficult; as a consequence, transportation agencies are experiencing challenges in managing timber bridges. One of the notable drawbacks associated with present practices is that the condition of timber is not considered in a realistic manner; scilicet, actual properties are not reflected and internal damage is not taken into account. It is hence unclear whether in-situ inspections are overly conservative, reasonable, or inadequate. Another concern is that, since inspections are heavily reliant upon the experience of field engineers, discrepant condition ratings are often reported (Li and Harris 2021). Technical information quantified by various nondestructive test methods can address these issues and generate unbiased outcomes, which would facilitate decision-making processes. This research elaborates on a practical approach related to the condition rating of timber bridges using visual inspections combined with nondestructive testing through the application of a machine learning algorithm.

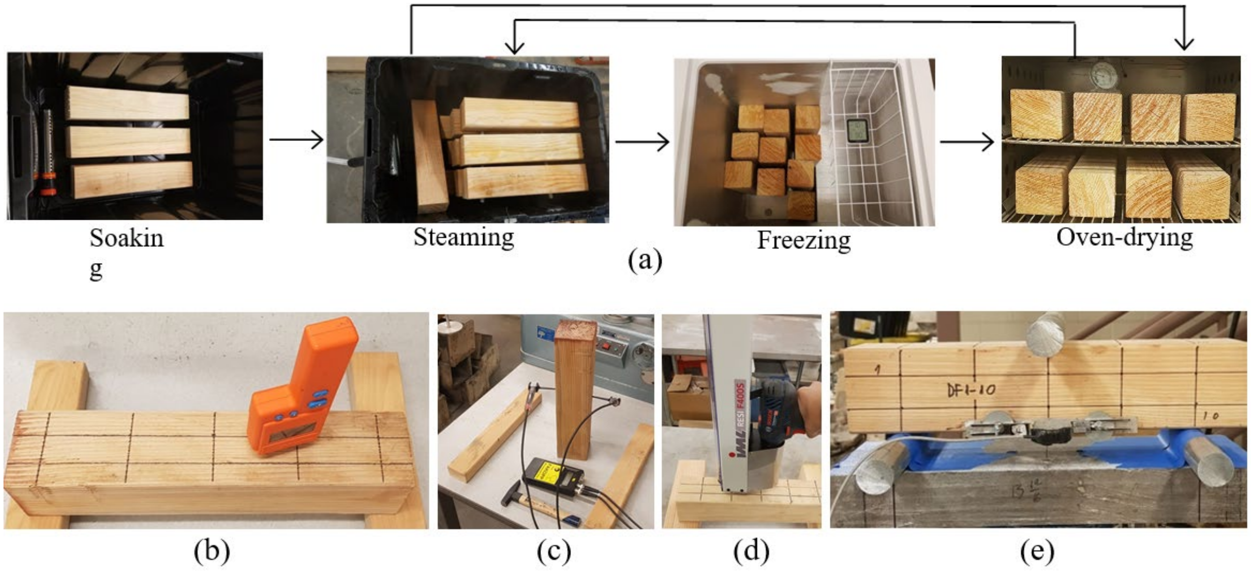

Fig. II.1. Laboratory testing: (a) protocol of ASTM D6874-21 (ASTM 2021); (b) moisture meter; (c) stress wave timer; (d) microdrill; (e) three-point bending

II.3. Prior Studies on Nondestructive Testing

An experimental program was conducted to predict the degree of deterioration in structural timber based on nondestructive tests (Kim and Ha 2024). Conforming to the procedural protocol of ASTM D1037 (ASTM 2020), 40 Douglas Fir beams were conditioned under soaking, steaming, freezing, and oven-drying environments for up to 288 hours (Fig. II.1(a)). After completing the accelerated exposure schemes, three nondestructive test methods were applied (i.e., moisture metering, stress wave timing, and microdrilling, Figs. II.1(b) through (d)) to investigate the physical response of the specimens; then, the acquired data were correlated with findings from destructive assessments (Fig. II.1(e)). Ancillary testing was also carried out for the clarification of the test results, namely, digital microscopy and rebound hammering. The succeeding expressions were established:

$$E = \rho V^2 \tag{II.1}$$

$$D_R = 2.22\left(V_R\right)^{0.84} \tag{II.2a}$$

$$V_R = \frac{\left(V_{cont} - V_{\det}\right)}{V_{cont}} \times 100 \text{ with } V_{det} \leq V_{cont} \tag{II.2b}$$

$$D_R = 3.9\left(W_R\right)^{0.59} \tag{II.3a}$$

$$W_R = \frac{\left(W_{\det} - W_{cont}\right)}{W_{cont}} \times 100 \text{ with } W_{cont} \leq W_{det} \tag{II.3b}$$

$$D_R = 26.8\left(R_R\right)^{0.075} \tag{II.4a}$$

$$R_R = \frac{\left(R_{cont} - R_{\det}\right)}{R_{cont}} \times 100 \text{ with } R_{det} \leq R_{cont} \tag{II.4b}$$

where E_{dyn} is the elastic modulus of the specimens; ρ is the density of the timber (an average density of ρ = 31.5 lb/ft^3 may be used); V is the velocity of the stress wave; D_R is the deterioration ratio of the timber (D_R = 0%: undamaged and D_R > 0%: damaged); V_{cont} and V_{det} are the velocities of the intact and deteriorated specimens, respectively; and W_{cont} and W_{det} and R_{cont} and R_{det} are their stress wave timing and drilling resistance, respectively. The baseline values of V_{cont} = 4,467 ft/sec., W_{cont} = 2,408 microsec./ft, and R_{cont} = 70.7% were recommended. Practice guidelines stated three deterioration states: Good (0% < $D_R \leq$ 15%), Moderate (15% < $D_R \leq$ 20%), and Fair (20% < $D_R \leq$ 30%).

Table II.1. Condition rating scale of the National Bridge Inventory (NBI)

Rating	Condition	Description
9	Excellent	Bridge elements are in an excellent condition
8	Very good	No problem noted
7	Good	Some minor problems
6	Satisfactory	Structural elements show some minor deterioration.
5	Fair	All primary structural elements are sound but may have minor section loss, cracking, spalling or scour
4	Poor	Advanced section loss, deterioration, spalling or scour
3	Serious	Loss of section, deterioration, spalling, or scour have seriously affected primary structural components. Local failures are possible. Fatigue cracks in steel or shear cracks in concrete may be present
2	Critical	Advanced deterioration of primary structural elements. Fatigue cracks in steel or shear cracks in concrete may be present or scour may have removed substructure support. Unless closely monitored it may be necessary to close the bridge until corrective action is taken
1	Imminent failure	Major deterioration or section loss present in critical structural components or obvious vertical or horizontal movement affecting structure stability. Bridge is closed to traffic but corrective action may put back in light service
0	Failed	Out of service - beyond corrective action

Table II.2. Configuration of timber bridges

Bridge ID	Bridge No.	Year built	Span (ft)	Width (ft)	Deck*	Super.*	Sub.*	Overall*
D-19-A	1	1936	22.5	31	5	4	5	Poor
D-18-B	2	1952	22.5	31	8	4	6	Poor
K-18-AD	3	1936	22.5	76	6	4	6	Poor
M-16-Q	4	1957	22.5	31	6	5	4	Poor
F-20-C	5	1931	26.2	31	4	4	5	Poor
F-19-C	6	1932	27.0	31	5	6	6	Fair
H-19-K	7	1935	22.9	30	6	5	6	Fair
H-20-P	8	1935	22.9	30	6	5	6	Fair
H-20-Q	9	1935	22.9	30	6	6	6	Fair
H-20-T	10	1935	22.5	31	6	6	6	Fair

ID = identification; No. = number; Span = maximum span length; Width = deck width; Super. = superstructure; Sub. = substructure

*: conditioning rating (visual inspection) determined by the Colorado Department of Transportation

Fig. II.2. Visual inspection of timber bridges: (a) D-18-B; (b) K-18-AD; (c) M-16-Q; (d) F-20-C; (e) F-19-C; (f) H-19-K

II.4. Constructed Bridges

Guided by the Colorado Department of Transportation (CDOT), candidate bridges were identified with condition states in either Fair or Poor (Table II.1, FHWA 2014). Table II.2 describes the configuration of the bridges. The span and width of the bridges varied from 22.5 ft to 27.0 ft and 30 ft to 76 ft, respectively, with year-built of 1931 to 1957. The condition rating of most load-bearing members was equal to or less than 6 (*Satisfactory*, Table II.1). Pictured in Fig. II.2 are selected images taken from the inspected bridges. The D-18-B bridge with a superstructure rating of 4 (*Poor*, Table II.1) demonstrated several checks (Fig. II.2(a)). Such defects often take place when environmentally induced stresses are greater than the tensile resistance of wood perpendicular to the direction of grains (Baranski et al. 2020). Repeated wetting-and-drying is known to be a critical source of checks (Rashidi et al. 2021) and the State of Colorado undergoes considerable changes in seasonal weather (Ford et al. 2021). The occurrence of checks expedites moisture ingress, which can accelerate the deterioration of the girders (Rashidi et al. 2021). Maintenance activities like epoxy injections may be necessary to extend the longevity of aged bridges, contingent upon the size of checks. Whereas there are no globally accepted provisions, cursory guidelines are found in literature mentioning that the depth of checks less than one quarter of the member thickness is tolerable (TFEC 2018). The deteriorated K-18-AD bridge (Fig. II.2(b)) exhibited significant surface decay in the girders due to aggressive weathering and corrugated appearances were evident with discoloring. The predominant concern stemmed from the fact that part of the girders was noticeably damaged because of the interaction between environmental and mechanical stresses and those were repaired using lag bolts (Fig. II.2(b), inset).

Figures II.2(c) and (d) depict Poor-condition bridges (M-16-Q and F-20-C) that have been repaired. The superstructure rating of these bridges was 5 and 4 (*Fair* and *Poor*, Table II.1), respectively. The integrity of the girders in the M-16-Q bridge was enhanced by lag bolts (Fig. II.2(c), inset), and the capacity of the F-20-C bridge was upgraded using bolted steel strips (Fig. II.2(d), inset). Taking into account practicality and constructability, these rehabilitation methods are frequently adopted by transportation authorities (Ritter 1990). It should, however, be noted that repair with steel elements is not a sustainable solution because of corrosion; hence, the use of non-metallic materials (e.g., fiber reinforced polymer composites) is expected to offer an alternative strategy for dealing with durability problems (Saad and Lengyel 2022). The condition of the Fair bridges (F-19-C and H-19-K in Figs. II.2(e) and (f), respectively) was relatively sound with no serious damage, although the girders of H-19-K showed signs of wear.

II.5. Nondestructive Test Results

Delineated below are the results compiled from site work, encompassing the amount of moisture in timber girders, wave-transmission characteristics, and resistance against perforation. For nondestructive testing, ten locations are randomly chosen per girder (five accessible girders per bridge) and responses are recorded. The deterioration levels of the above-explained benchmark bridges are diagnosed and implementable instructions are outlined.

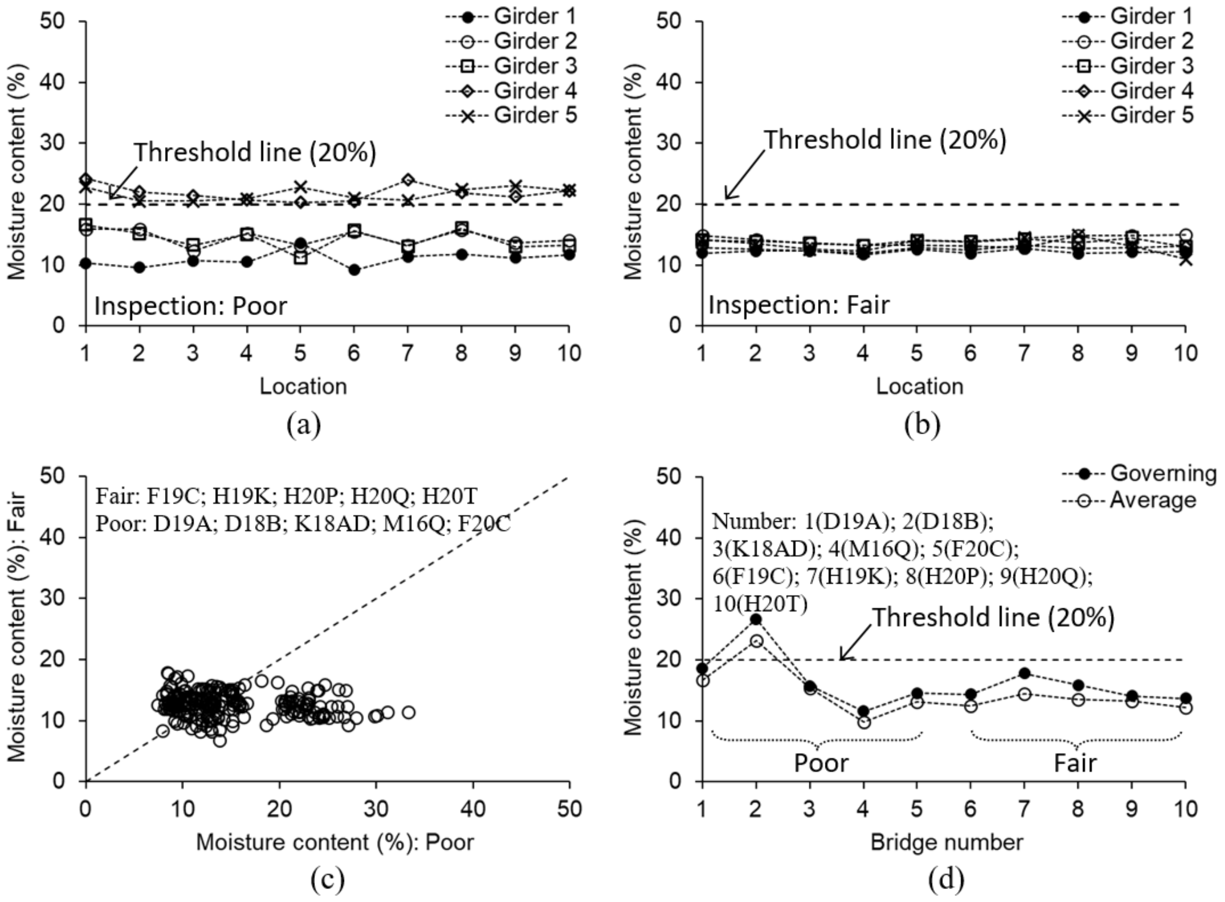

Fig. II.3. Moisture content: (a) D-19-A; (b) H-20-Q; (c) comparison between Poor and Fair bridges; (d) individual bridge response

II.5.1. Moisture content

The moisture content of the D-19-A (Poor) and H-20-Q (Fair) bridges is visible in Figs. II.3(a) and (b), respectively. According to published information (USDA 2010), a moisture limit of 20% was set to the threshold dividing endurable and decay-prone domains. For D-19-A, the moisture contents of Girders 4 and 5 were 8.8% higher than the threshold value, on average, whereas those of other girders were lower than the limit (Fig. II.3(a)). On the contrary, the contents of all girders in H-20-Q were steady with an average deviation of 34.7% from the limit (Fig. II.3(b)). These observations corroborate the fact that the amount of moisture greater than an acceptable boundary promotes insect infestation and precipitates the swelling of hydrophilic components (e.g., cellulose and hemicellulose), thereby decreasing the strength of wood (Hill et al. 2021). Figure II.3(c) compares the moisture contents of all inspected girders in the bridges with Poor and Fair conditions. Albeit scattered, the amount of moisture in the Poor bridges tended to be more than their Fair counterparts. Furthermore, this inclination is confirmed by the moisture contents of the individual bridges in Fig. II.3(d), where the maximum measured (governing) and mean (average) values are graphed. It is consequently stated that monitoring the level of moisture can assist in evaluating the condition of timber bridges when combined with other nondestructive test results: as evidenced in Fig. II.3(d), relying on moisture contents alone does not seem sufficient especially for rating timber bridges in poor condition.

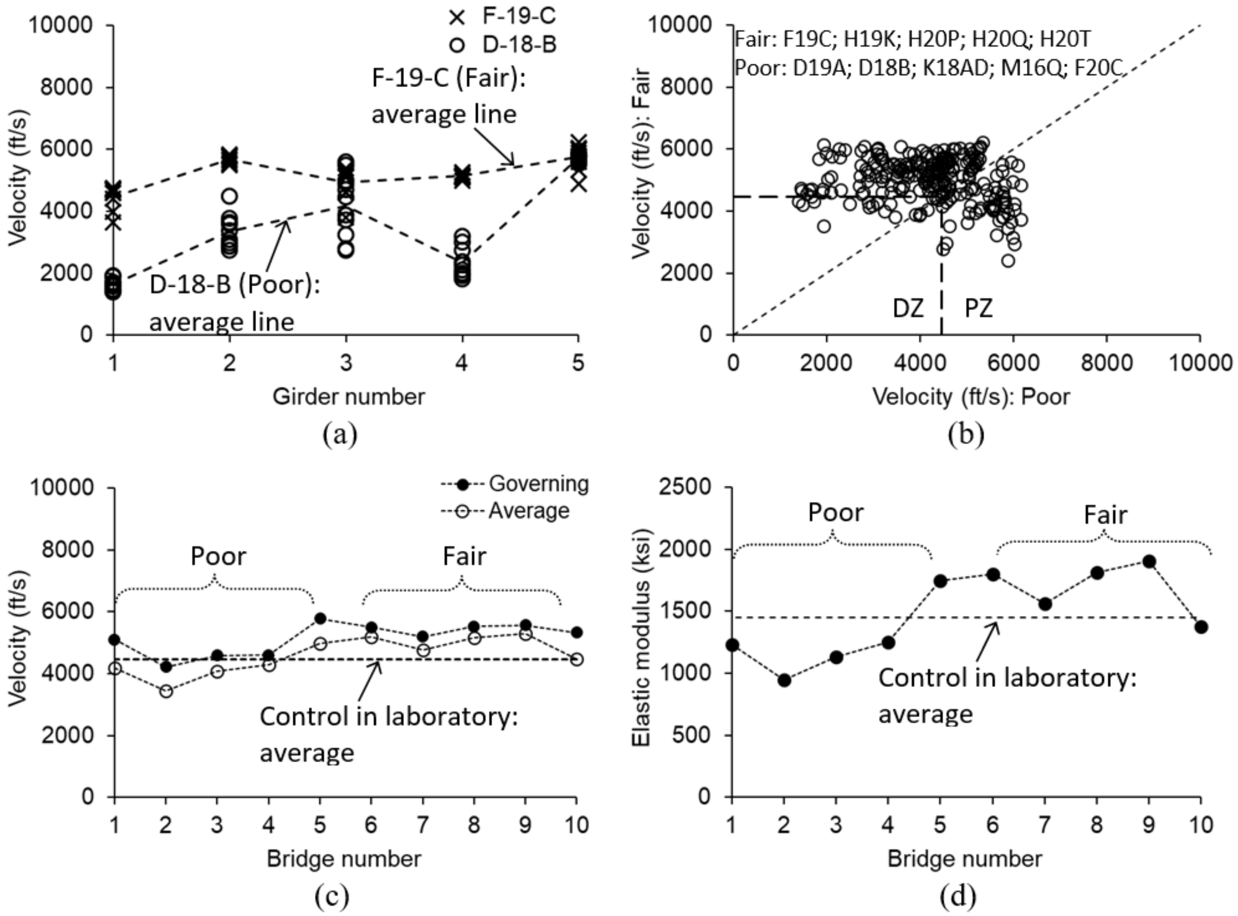

(a) (b)

(c) (d)

Fig. II.4. Velocity (PZ = pristine zone; DZ = deteriorated zone): (a) individual response; (b) comparison between Poor and Fair bridges; (c) individual bridge response; (d) elastic modulus

II.5.2. Velocity

Shown in Fig. II.4(a) is the velocity of stress waves for D-18-B (Poor) and F-19-C (Fair). The measured responses of F-19-C generally surpassed those of D-18-B and, dissimilar to the former, the latter revealed remarkable fluctuations among the girders. The inconsistent data for D-18-B point out that internal damage was irregular; in other words, voids and delamination randomly distributed throughout the interior of the deteriorated bridge hindered the progression of the stress waves (Pahnabi et al. 2024). In the context of microstructural reactions, impaired cellulosic crystalline tracheids in the wood cells dissipated energy and disrupted the transmission of acoustic signals (Bucur 2006; Lazarus et al. 2020). Owing to the erratic response of the damaged bridge girders, apparent disparity was not noticed between the Poor and Fair bridges (Fig. II.4(b)) and a significant portion of the measured velocities were in the pristine zone (PZ), rather than in the deteriorated zone (DZ), which was partitioned by the baseline velocity of V_{cont} = 4,467 ft/sec. Nonetheless, the average velocities of the Poor bridges were by and large slower (Fig. II.4(c)). The elastic moduli of the bridges converted from the average velocities using Eq. II.1 are given in Fig. II.4(d). The moduli oscillated around the modulus of undamaged timber tested in the laboratory (10 GPa) and the range of variation closely paralleled to the values for Douglas Fir, 1,160 ksi to 1,940 ksi, specified in the wood handbook of the United States Department of Agriculture (USDA 2010). In contrast to other bridges rated as Poor, the properties of Bridge No. 5 (F-20-C) were comparable to those of the bridges rated as Fair (Figs. II.4(c) and (d)).

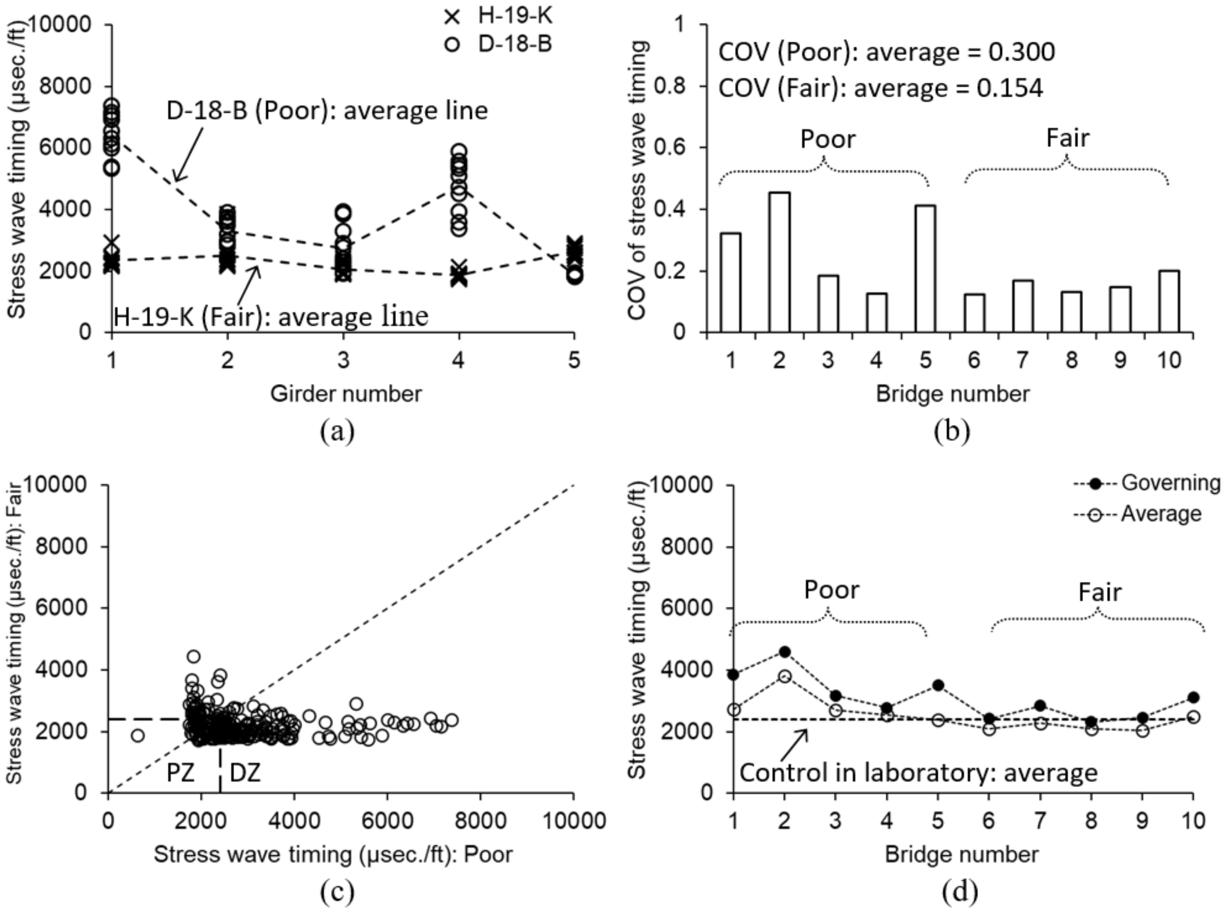

Fig. II.5. Stress wave timing (PZ = pristine zone; DZ = deteriorated zone): (a) individual response; (b) coefficient of variation (COV); (c) comparison between Poor and Fair bridges; (d) individual bridge response

II.5.3. Stress wave timing

Figure II.5(a) exhibits the stress wave timing of D-18-B (Poor) and H-19-K (Fair). Aligning with prior discussions, the wave-timing spectrum for the girders of the Fair bridge was stable in comparison with the spectrum for the Poor bridge. Figure II.5(b) supports this assertion through the coefficient of variation (COV). The average COV of the bridges rated in Poor condition was 194.8% higher than that of the bridges in Fair condition (COV = 0.300 vs. 0.154). The wide dispersion reaffirms that uncertainties in the degraded bridges arose from disordered microscopic discontinuities and softened substances within the degenerated wood cells (Neimz et al. 2023). Overall, the stress wave timing was apt to increase as the condition of the bridges aggravated in the deteriorated zone (Fig. II.5(c)), especially discernable when utilizing the governing values (Fig. II.5(d)).

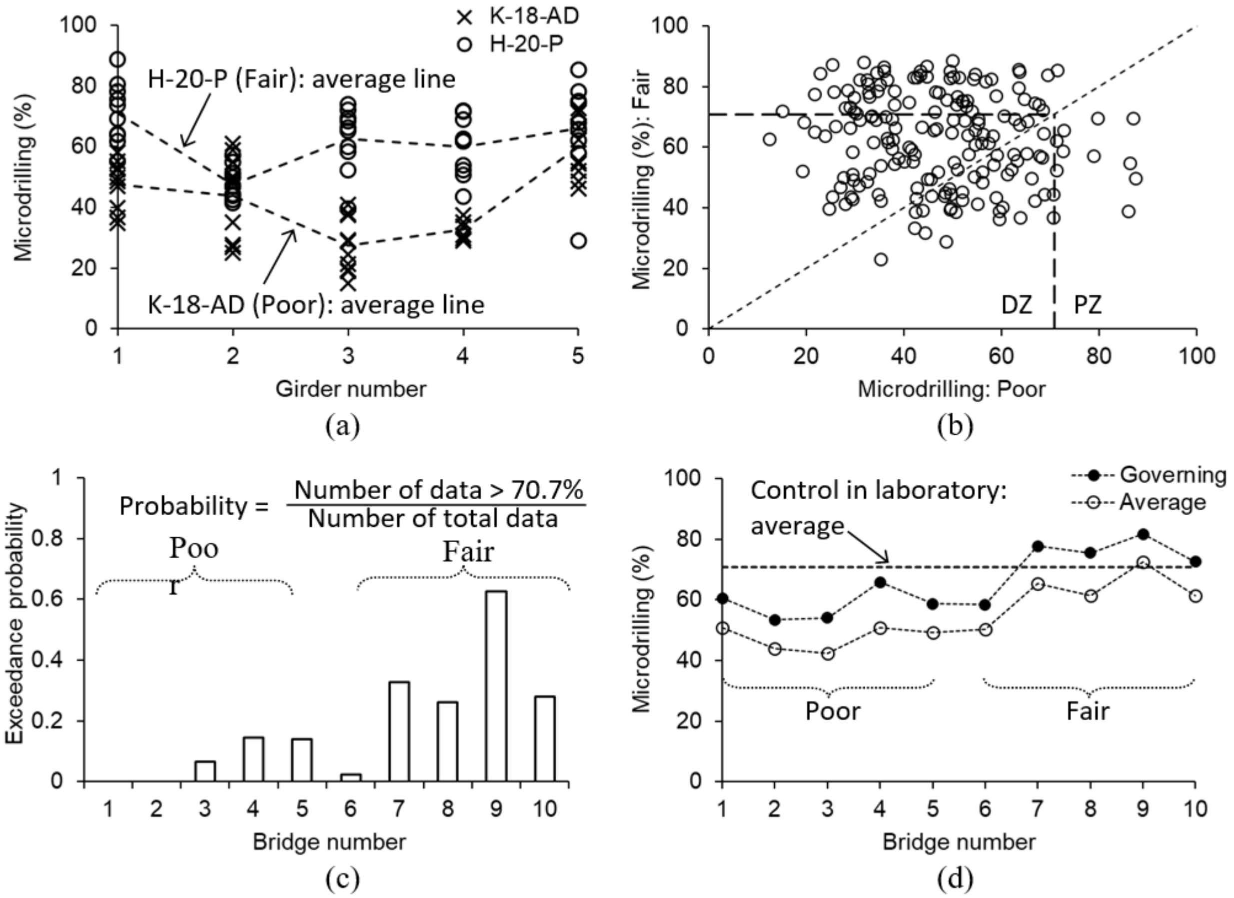

Fig. II.6. Microdrilling (PZ = pristine zone; DZ = deteriorated zone): (a) individual response; (b) comparison between Poor and Fair bridges; (c) exceedance probability; (d) individual bridge response

II.5.4. Microdrilling

The drilling resistance of typical bridges is instantiated in Fig. II.6(a). The disorganized data pattern of the bridges is attributed to the nonhomogeneous nature of the timber with irregularly distributed vessels and parenchyma cells (Pournou 2020). For the Fair bridge (H-20-P), the average drilling resistance was 61.5% with a minimum value of 47.7% in Girder 2 presumably due to local deterioration. Contrarily, the average resistance of the Poor bridge (K-18-AD) was 42.3%, verifying that the structure of decomposed cell walls contributed to the physical degradation of the bridge assigned a superstructure rating of 4 (Ayanleye et al. 2022). The extent of spreading was substantial when analyzing the data points of the Fair and Poor bridges (Fig. II.6(b)) and a significant fraction of them were under the threshold of 70.7% (the DZ region). Figure II.6(c) shows the exceedance probability of the drilling resistance. The average exceedance probability of the Poor (Nos. 1 to 5) and Fair (Nos. 6 to 10) bridges was 0.07 and 0.31, respectively. This means that, even with the large dispersion, microdrilling can be recognized as a viable technique for classifying the condition of in-situ bridges, particularly using the governing resistance values rather than the average ones (Fig. II.6(d)).

II.5.5. Level of Deterioration

The deterioration level for all bridges was calculated using the acoustic signals in conjunction with Eqs. II.2 to 4 and is plotted in Fig. II.7. As portrayed in Fig. II.7(a), the degree of deterioration varied among the girders and differed across the randomly selected sampling locations. Figure II.7(b) illustrates the deterioration levels of the governing girders from four bridges. Despite the uneven responses of the girders, the bridges labeled as Poor (D-19-A and D-18-B) displayed markedly greater deterioration relative to the ones labeled as Fair (H-19K and H-20-T). To effectively represent such variable deterioration levels, the governing and average values extracted from the stress wave timing (Fig. II.7(c)), velocity (Fig. II.7(d)), and microdrilling (Fig. II.7(e)) data were employed. Contrary to the stable predictions of the microdrilling, minor discrepancies were seen between the readings given in Figs. II.7(c) and (d), meaning that Eqs. II.2 and 3 are suitable for practice. The gross mean of the governing deterioration ratios (arithmetic average of Eqs. II.2(a), 3(a), and 4(a)) is provided in Fig. II.7(f). The deterioration of certain bridges with a visual inspection rating of Poor (No. 1 to 5) was positioned above the Fair limit of D_R = 30%; by contrast, that of the bridges with a visual inspection rating of Fair (No. 6 to 10) consistently remained below the 30% limit. This fact signifies that, under the threshold limit of D_R = 30%, the laboratory-based performance classification can distinguish between Fair and Poor conditions observed during site inspections and that some bridges in Poor condition were conservatively rated and conducting nondestructive tests could have facilitated appropriate inspection decisions.

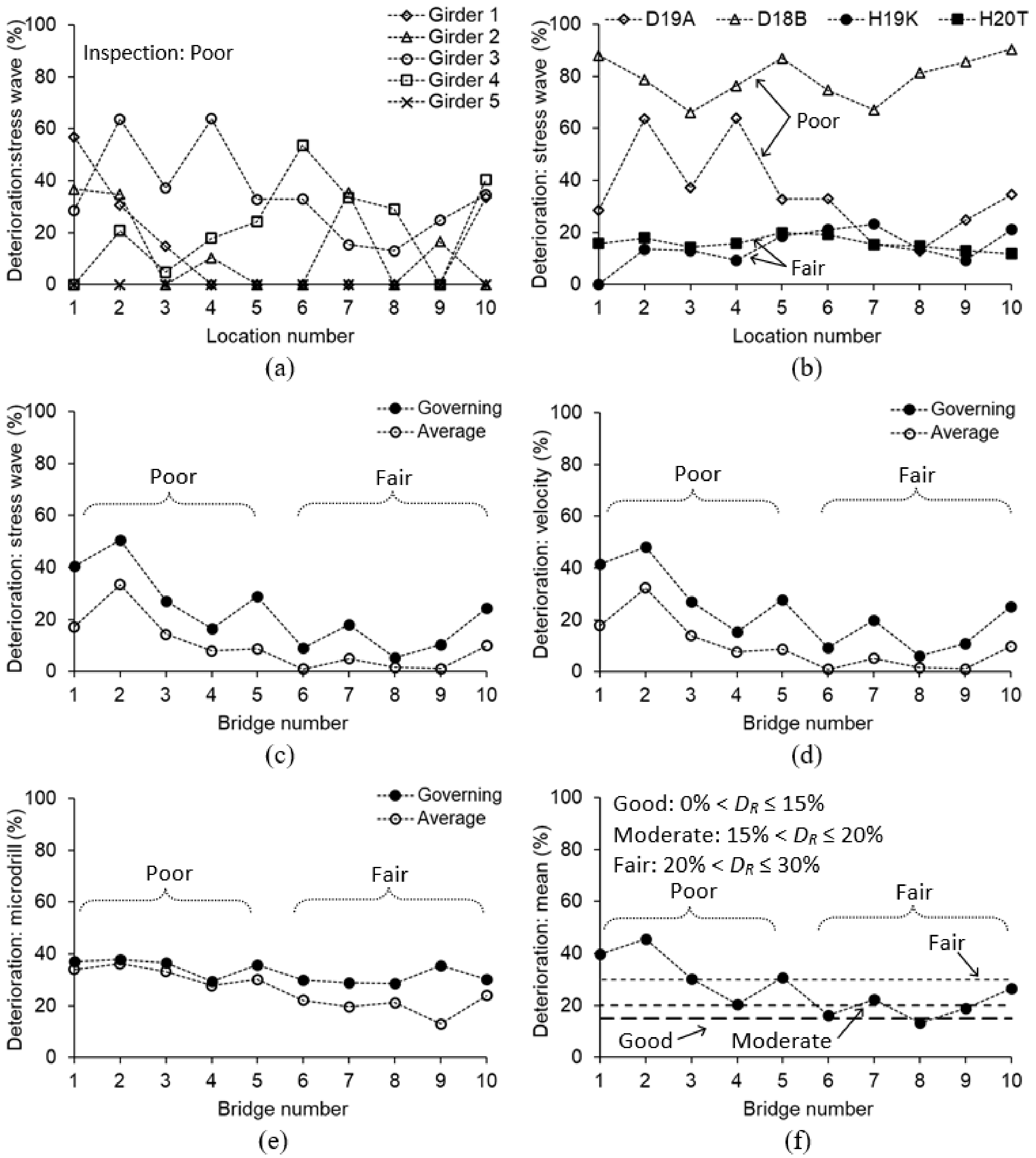

Fig. II.7. Predicted deterioration level: (a) D-19-A; (b) selected girders; (c) overall comparison based on stress wave timing; (d) overall comparison based on velocity; (e) overall comparison based on microdrilling; (f) mean based on governing cases

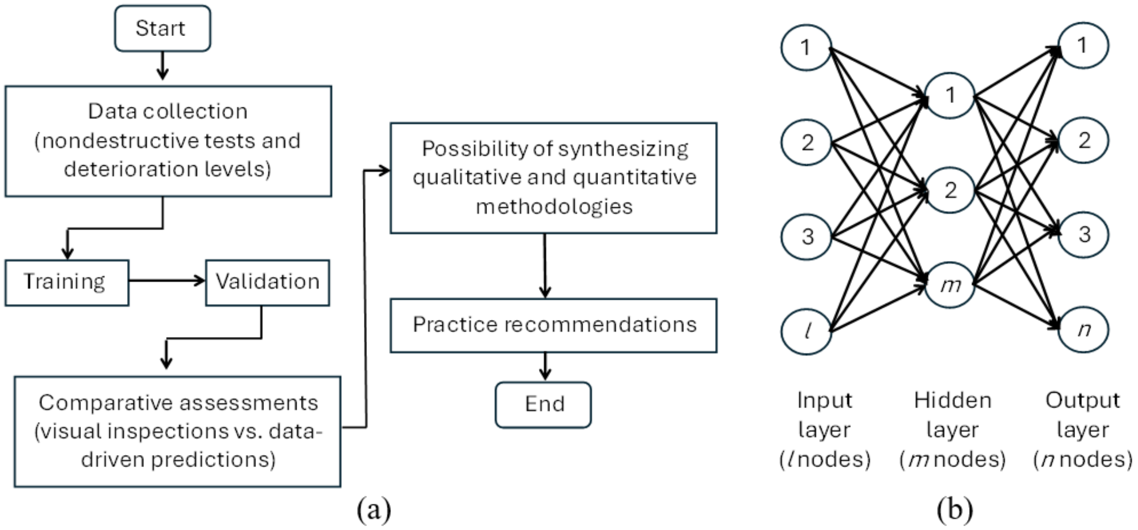

Fig. II.8. Computational modeling: (a) flowchart; (b) concept of multilayer neural networks

II.6. Computational Modeling

A machine learning framework is deployed to predict the deterioration levels of timber bridges in line with those determined by nondestructive tests. Figure II.8(a) presents a flowchart of the computational framework with a focus on sequential phases and reproducible features, enabling the integration of qualitative and quantitative inspection approaches.

II.6.1. Machine learning

Among the numerous established algorithms in machine learning, the platform of neural networks was chosen for its popularity and precision (Ekman 2021). A conceptual description is synopsized herein, while the theory and problem-solving procedures of neural networks can be found elsewhere (Mehlig 2022). Neural networks, comprising input, hidden, and output layers, are formed with interconnected artificial entities (called neurons) that operate on a massive amount of computed data (Fig. II.8(b)). The fundamental mechanism of computation is that the algorithm minimizes errors between predicted and target values by means of a loss function (Eq. II.5 was used for the present study, Bishop and Bishop 2024).

$$F_{loss} = \frac{1}{2\sigma^2}\sum_{n=1}^{N}\left\{y\left(x_n,w\right)-t_n\right\}^2 + \frac{N}{2}\ln\sigma^2 + \frac{N}{2}\ln\left(2\pi\right) \qquad \text{(II.5)}$$

where F_{loss} is the loss function; N is the number of the data points; σ^2 is the variance; $y(x_n,w)$ *is* the predicted output for the input x_n; w is the model parameter; and t_n is the target value for x_n. The supervised processing algorithm, built upon input and output datasets from the timber bridges (nondestructive test results and condition ratings, respectively), was trained and validated using 80% and 20% of the site-supplied measurements. Such dataset allocation percentage is broadly applied in the bridge engineering community (Liu and Zhang 2020). Once the model was fully trained (i.e., the adaptive system stabilized its performance refinement through iterations), it inferred values for data from outside the acquainted set. The computed deterioration ratios of the benchmark bridges are rendered in Fig. II.9. The distance of the individual data points from the one-to-one line was interpreted as an evaluation metric, called residuals, to ascertain the relative performance of predictions against the site-based deterioration ratios. It is worth noting that the residual values in Fig. II.9 do not mean that one nondestructive test method is acceptable while others are inferior; instead, the values merely demonstrate the relative effectiveness of the three nondestructive test approaches. The residuals of the velocity-driven deterioration ratios (Figs. II.9(a) and (d)) were smaller than others, and the bridges rated as Poor (Figs. II.9(a) to (c)) manifested higher residuals compared with those rated as Fair (Figs. II.9(d) to (f)). These results illustrate that integrating predicted deterioration ratios from the three nondestructive test techniques can generate reliable outcomes by offsetting their disparities, notably beneficial for the Poor-rated bridges.

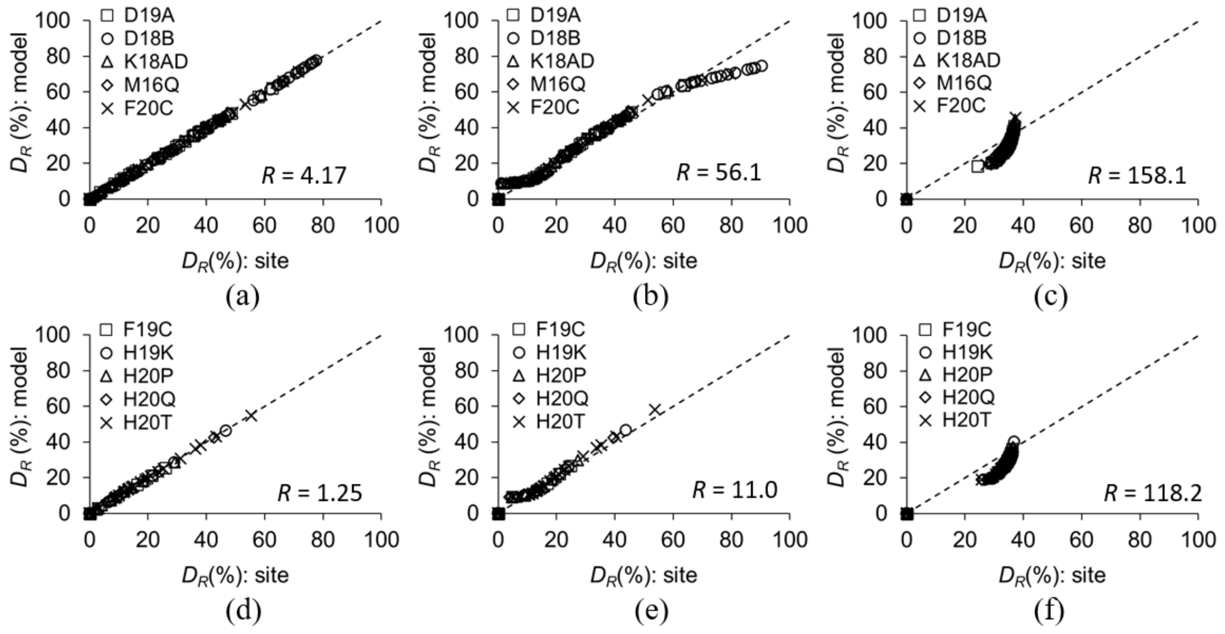

(a) (b) (c)

(d) (e) (f)

Fig. II.9. Deterioration ratio from machine learning model and site data (*R* = residual): (a) velocity in Poor bridges; (b) stress wave timing in Poor bridges; (c) microdrilling in Poor bridges; (d) velocity in Fair bridges; (e) stress wave timing in Fair bridges; (f) microdrilling in Fair bridges

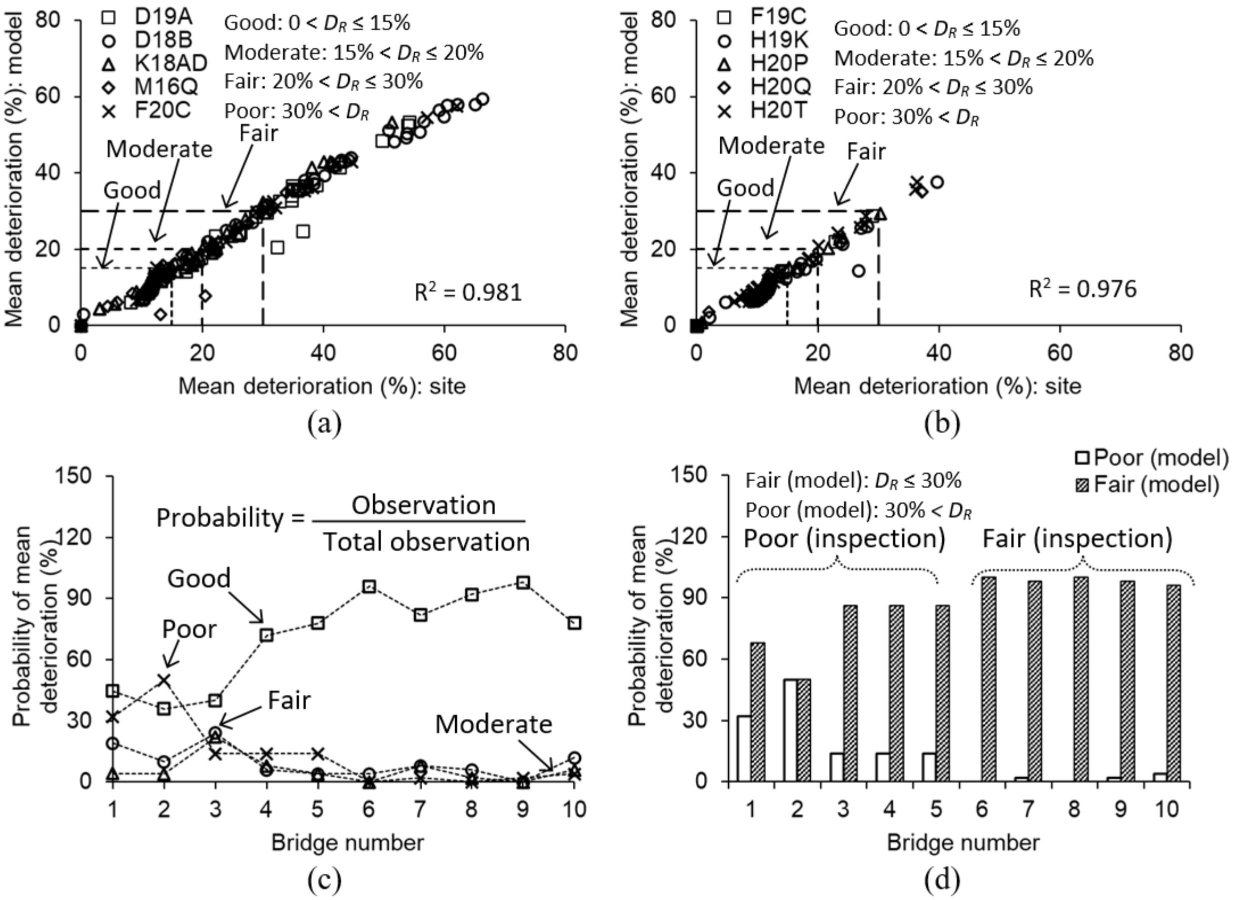

(a) (b) (c) (d)

Fig. II.10. Assessment of mean deterioration (R^2 = coefficient of determination): (a) comparison of model and site data for bridges rated as Poor; (b) comparison of model and site data for bridges rated as Fair; (c) probability of predicted mean deterioration; (d) overall prediction

II.6.2. Implementation

Figures II.10(a) and (b) correlate the mean deterioration ratios of the bridges rated as Poor and Fair, respectively. In addition to the three deterioration states of Good, Moderate, and Fair, the Poor category ($30\% < D_R$) was presented for comparison purposes with the visual inspection ratings. The model predictions from the machine learning method matched the site data obtained from the nondestructive tests with the coefficients of determination of $R^2 = 0.981$ (Fig. II.10(a)) and 0.976 (Fig. II.10(b)). The occurrence probability of each deterioration state in the model predictions is shown in Fig. II.10(c). Even if the distribution of the Fair and Moderate states was below 24%, the Poor and Good states were conspicuous throughout. Figure II.10(d) charts a one-to-one appraisal of the visual inspection ratings versus model predictions with lump-summed classifications for Fair ($D_R \leq 30\%$) and Poor ($30\% < D_R$). For the bridges rated as Poor in the field (Nos. 1 to 5), both Fair and Poor ratings appeared in the model predictions; conversely, a consensus was reached for the bridges rated as Fair (Nos. 6 to 10). A plausible explanation for the discrepancies in the Poor-rated bridges is that the site ratings were more stringent and that the predicted ratings did not account for physical conditions at the structural level as the nondestructive tests focused on the material responses of the bridges. Therefore, a combination of these distinct approaches can yield accurate ratings for aged timber bridges.

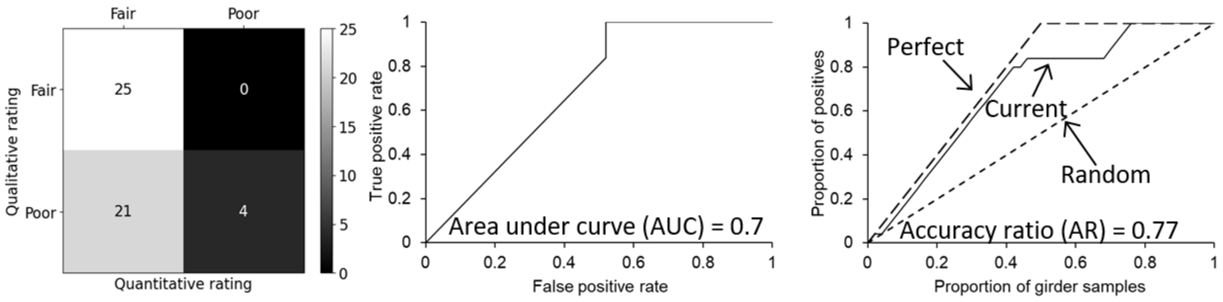

(a) (b) (c)

Fig. II.11. Qualitative vs. quantitative condition ratings: (a) confusion matrix; (b) receiver operating characteristic (ROC) curve; (c) cumulative accuracy profile (CAP) curve

II.6.3. Synthesis of inspection methodologies

Comparative investigations were performed to figure out the degree of conformity between the qualitative (visual) and quantitative (machine learning informed by nondestructive test data) ratings of the benchmark bridges, which are instrumental in synthesizing these inspection methodologies. Figure II.11(a) visualizes the effectiveness of categorization via a confusion matrix. Even though this graphical representation merely tallies specific events, it can readily correlate two independent classes (Campesato 2023). For the 50 girders of the ten benchmark bridges, the fractions of Fair-Fair and Poor-Poor ratings were 25/50 and 4/50, respectively, resulting in an agreement ratio of 29/50 or 58%. As expatiated in Fig. II.7, the inconsistency originates from the bridges rated as Poor (Nos. 1 to 5) during the visual inspections. To complement the basic correlation method, a receiver operating characteristic (ROC) curve was constructed with True Positive and False Positive Rates (TPR and FPR in Eqs. II.6 and 7, respectively, Bishop and Bishop 2024):

$$TPR = \frac{N_{TP}}{N_{TP} + N_{FN}} \tag{II.6}$$

$$FPR = \frac{N_{FP}}{N_{FP} + N_{TN}} \tag{II.7}$$

where N_{TP} is the number of true positives (Fair in visual and Fair in machine learning); N_{FN} is the number of false negatives (Fair in visual and Poor in machine learning); and N_{FP} is the number of false positives (Poor in visual and Fair in machine learning). The area under the curve (AUC) gauges a classifier's performance (AUC = 0.5: trivial classification and AUC = 1.0: error-free classification). In light of the fact that AUC ≥ 0.7 is commonly seen as acceptable performance (Mandrekar 2010), the AUC of 0.7 in Fig. II.11(b) indicates a satisfactory match between the qualitative and quantitative ratings. Figure II.11(c) provides an alternative assessment tool using a cumulative accuracy profile (CAP) curve. The abscissa and ordinate coordinates of the CAP curve were set by the proportions of girder samples (cumulated fractions of the 50 girders as the independent variable) and positives (cumulated fractions of the true positives as the dependent variable), respectively. The Perfect curve was drawn from the instance that correctly identified all positive cases and the Random curve was created by a 1:1 line symbolizing random performance. Instructional guides may be referenced in data analytics textbooks (Anderson 2022; Walker 2022). The accuracy ratio (AR) of the Current curve in Fig. II.11(c) was calculated by (Neisen and Geraskin 2022)

$$AR = \frac{A_R}{A_P} \tag{II.8}$$

where A_R is the area between the Current and Random CAP curves and A_P is the area between the Perfect and Random CAP curves. The accuracy ratio of AR = 0.77 was greater than the reasonable precision range of AR = 0.51 to 0.6 (Housni et al. 2019). In accordance with the analyses above, it is conclusively claimed that merging the qualitative and quantitative methods is plausible to synergistically improve rating procedures. That is, a mean deterioration ratio is calculated using governing deterioration ratios supplied by the three nondestructive test methods at no less than ten randomly selected locations ($D_R \leq 30\%$: Fair and $30\% < D_R$: Poor) and then the consequences of visual inspections at the structural scale (e.g., physical damage) are synthesized to inform a rating decision.

II.7. Determination of Condition Factor

To estimate the live-load-carrying capacity of inspected highway bridges, the Load and Resistance Factor Rating (LRFR) method is acknowledged as the norm in modern practices. Although the traditional Allowable Stress Rating (ASR) method is widespread for timber bridges, initiatives are in progress to move toward LRFR (IDOT 2013; RIDOT 2022). As part of such undertakings, the condition factor of LRFR (AASHTO 2017) is calibrated to address potential problems arising from the increased uncertainty in the resistance of degraded girders.

II.7.1. Derivation

Pursuant to the AASHTO Manual for Bridge Evaluation (AASHTO 2017), the rating equation of a load-bearing member is defined as

$$RF = \frac{C - \gamma_{DC} DC - \gamma_{DW} DW \pm \gamma_p P}{\gamma_{LL}\left(LL + IM\right)} \tag{II.9}$$

$$C = \Phi R_n = \phi_c \phi_s \phi R_n \tag{II.10}$$

where RF is the rating factor of the member; C is the factored capacity of the member; γ_{DC} and γ_{DW} are the dead load factors (γ_{DC} = 1.25 and γ_{DW} = 1.5) for the structural components (DC) and wearing surface (DW), respectively; γ_p is the factor (γ_p = 1.0) for the permanent load (P); γ_{LL} is the live load factor (γ_{LL} = 1.75); LL is the live load effect; IM is the dynamic load allowance; Φ is the LRFD resistance factor; ϕ_c, ϕ_s, and ϕ are the condition, system (ϕ_s = 1.0 for most girder bridges, AASHTO 2017), and strength reduction (ϕ = 0.85 for flexure, AASHTO 2017) factors, respectively; and R_n is the nominal capacity. Ignoring the wearing and permanent load terms in Eq. II.9, a performance function (g) may be expressed to be

$$g = C - \left\{DC + \left(LL + IM\right)\right\} \tag{II.11}$$

In compliance with published literature (Barker and Puckett 1997; Nowak 1999), the distribution types of the capacity (*C*) and load effects (*E* = *DC* or *LL*) may be taken as lognormal and normal, respectively. On the basis of reliability theory (Nowak and Collins 2013), the subsequent derivations are undertaken.

The equivalent normal parameters for R_n are written by

$$\mu_C^{eq} = x' \left\{1 - \ln\left(x' / \mu_{\ln C}\right)\right\} \quad \text{(II.12)}$$

$$\sigma_C^{eq} = x' COV_C \quad \text{(II.13)}$$

where μ_C^{eq} and σ_C^{eq} are the equivalent mean and standard deviation of the capacity, respectively; *x'* is the design point value; and COV_C is the coefficient of variation of the capacity. The partial derivatives of the performance function (G_i) along with the column vector {*α*} are given as

$$G_i = -\frac{\partial g}{\partial Z_i} \sigma_{Z_i} \quad \text{(II.14)}$$

$$\left\{\alpha_i\right\} = \frac{\left\{G_i\right\}}{\sqrt{\left\{G_i\right\}^T \left\{G_i\right\}}} \quad \text{(II.15)}$$

where Z_i is the variable ($Z_1 = C$ and $Z_2 = E$) and σ_{Zi} is the standard deviation. An updated design point (x_i') is provided by

$$x_i' = \mu_{Z_i} + \alpha_1 \beta \sigma_{Z_i} \quad \text{(II.16)}$$

where *β* is the safety index. The updated mean of the resistance (μ_C) and the LRFD resistance factor (Φ) are calculated using

$$\mu_C = \frac{x_i'}{1 + \alpha_C \beta COV_C} \quad \text{(II.17)}$$

$$\Phi = \frac{x_i'}{\mu_C} \tag{II.18}$$

Finally, the condition factor (ϕ_c) is attained

$$\phi_c = \frac{\Phi}{\phi_s \phi} \leq 1.0 \tag{II.19}$$

II.7.2. Proposal

To implement Eq. II.19, the COV values of the bridges were taken from literature (Nowak 1999; Barker and Puckett 1997; Kim and Ha 2024): COV = 0.156, 0.0264, and 0.18 for the nominal capacity, dead load, and live load, respectively. With successive iterations, the solutions for the condition factor converged (Fig. II.12(a)): three condition states (Good, Fair, and Poor) were designated to ensure conformity with the AASHTO bridge evaluation manual (AASHTO 2017). Since the level of safety is not constant but case-specific, varying safety indexes were considered from β = 2.0 to 3.5. The condition factor was consistent at ϕ_c = 1.0 for the Good state; however, as the bridge condition deteriorated, variations were noted (Fig. II.12(b)). Table II.3 lists the proposed condition factors reflecting structural conditions and safety levels, which can be used for rating aged timber bridges.

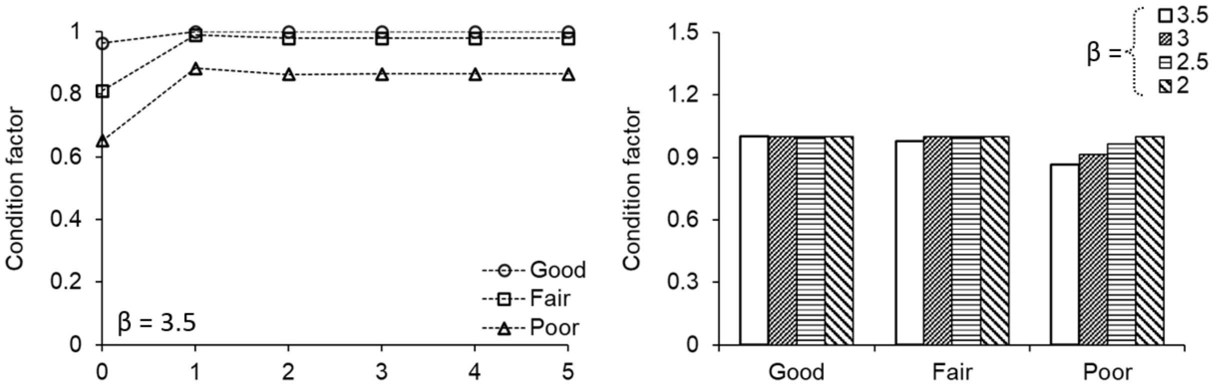

(a) (b)

Fig. II.12. Calibration of condition factor for timber bridges: (a) convergence; (b) variable reliability index

Table II.3. Proposed condition factor (ϕ_c) for timber bridges

Safety level	Structural condition of member		
	Good	Fair	Poor
$\beta = 3.5$	1.00	0.95	0.85
$\beta = 3.0$	1.00	1.00	0.90
$\beta = 2.5$	1.00	1.00	0.95
$\beta = 2.0$	1.00	1.00	1.00

II.8. Summary and Conclusions

This research has explored the performance evaluation of timber bridges through visual inspections and nondestructive testing with the goal of unifying these qualitative and quantitative methodologies. The condition of ten benchmark bridges, visually rated as Poor and Fair, was studied by moisture metering, stress wave analysis, and microdrilling techniques, leading to the determination of their deterioration levels. The next step involved training a machine learning algorithm to discern compatibility between ratings from the qualitative and quantitative approaches. For the execution of Load and Resistance Factor Rating (LRFR), condition factors were calibrated under diverse operational environments. The following conclusions are drawn:

- The moisture content of the bridges rated as Poor was usually greater than that of the bridges rated as Fair. The threshold limit of 20% for moisture content was well-suited as a preliminary metric to differentiate between these bridge classifications.
- The travel velocity of stress waves depended upon the degree of internal damage in timber girders. Relative to the case of the Fair-rated bridges, the velocities of the Poor-rated bridges were inclined to be slower and a baseline velocity of 4,467 ft/sec. was set as the demarcation value. The elastic moduli of the girders were approximately 1,450 ksi, underscoring that in-situ deterioration had minimal impact on the serviceability (deflection) of the bridges.
- Regarding stress wave timing, a stable pattern was seen for the Fair-rated bridges; however, appreciable fluctuations were noted for the Poor-rated bridges, as indicated by their respective COV values of 0.154 vs. 0.300. An increasing propensity was obvious for the magnitude of the wave timing beyond 2,408 microsec./ft when the condition of the bridges worsened.

- The diminution of drilling resistance in the Poor-rated bridges was more than 31% compared with the Fair-rated ones. The probability of exceeding the baseline resistance of 70.7% was 0.07 and 0.31 for the Poor and Fair bridges, respectively, on average. Microdrilling proved to be an applicable technique for examining the condition of timber bridges.
- The deterioration level of the bridges rated as Poor by visual inspections was not always consistent with the levels calculated by the nondestructive testing, whereas compatibility was achieved for the Fair category. The necessity for a refined rating guideline was thus highlighted and suggestions were put forward.
- The machine learning model validated by the coefficient of determination of over $R^2 = 0.976$ was coupled with various performance classification methods. Investigations substantiated that leveraging the visual inspections (qualitative) alongside the data-driven methodologies (quantitative) would ameliorate the rating procedure for aged timber bridges. The proposed condition factors in relation to structural conditions (Good, Fair, and Poor) and safety levels ($\beta = 2.0$ to 3.5) are recommended for practical application.

II.9. References

AASHTO. 2017. The manual for bridge evaluation (3rd edition), American Association of State Highway and Transportation Officials, Washington, D.C.

AASHTO. 2020. AASHTO LRFD bridge design specifications (9th edition), American Association of State Highway and Transportation Officials, Washington, D.C.

Abdallah, A.M., Atadero, R.A., and Ozbek, M.E. 2021. A state-of-the-art review of bridge inspection planning: current situation and future needs, Journal of Bridge Engineering, 27(2), 0312100.

Anderson, R.A. 2022. Credit intelligence and modelling, Oxford University Press, Oxford, UK.

ARTBA. 2023. Bridge report, American Road & Transportation Builders Association, Washington, D.C.

ASTM. 2020. Standard test methods for evaluating properties of wood-base fiber and particle panel materials (ASTM D1037-12), ASTM International, West Conshohocken, PA.

ASTM. 2021. Standard test methods for nondestructive evaluation of the stiffness of wood and wood-based materials using transverse vibration or stress wave propagation (ASTM D6874-21), ASTM International, West Conshohocken, PA.

Ayanleye, S., Udele, K., Nasir, V., Zhang, X., and Militz, H. 2022. Durability and protection of mass timber structures: a review, Journal of Building Engineering, 46, 103731.

Baranski, J., Konopka, A., Vilkovska, T., Klement, I., and Vilkovsky, P. 2020. Deformation and surface color changes of beech and oak wood lamellas resulting from the drying process, BioResources, 15(4), 8965-8980.

Barker, R.M. and Puckett, J.A. 1997. Design of highway bridges, John Wiley & Sons, Inc. New York, NY.

Bishop, C.M. and Bishop, H. 2024. Deep learning: foundations and concepts, Springer, Cham, Switzerland.

Brashaw, B., Wacker, J., and Ross, R.J. 2014. Advanced timber bridge inspection, Natural Resources Research Institute, University of Minnesota Duluth, Duluth, MN.

Bucur, V. 2006. Acoustics of wood, Springer, Berlin, Germany.

Campesato, O. 2023. Statistics using Python, Mercury Learning and Information, Boston, MA.

Ekman, M. 2021. Learning deep learning, Pearson Education, London, UK.

FHWA. 2014. National bridge inventory (NBI) based on the coding guide, Federal Highway Administration, Washington, D.C.

Ford, T.W., Chen, L., and Schoof, J.T. 2021. Variability and transitions in precipitation extremes in the Midwest United States, Journal of Hydrometeorology, 22, 533-545.

Hill, C., Altgen, M., and Rautkari, L. 2021. Thermal modification of wood- a review: chemical changes and hygroscopicity, Journal of Materials Science, 56, 6581-6614.

Housni, M., Namir, A., Talbi, M., and Chafiq, N. 2019. Applying data analytics and cumulative accuracy profile (CAP) approach in real-time maintenance of instructional design models, Lecture Notes in Real-Time Intelligent Systems (RTIS 2017), 17-25.

IDOT. 2013. Bridge rating manual, Iowa Department of Transportation, Ames, Iowa.

Kim, Y.J. and Ha, T. 2024. Nondestructive and destructive tests for damage quantification of deteriorated structural timber, Engineering Structures, Manuscript No. ENGSTRUCT-S-24-07680.

Lazarus, B.S., Velasco-Hogan, A., Gomex-del Rio, T., Meyers, M.A., and Jasiuk, I. 2020. A review of impact resistant biological and bioinspired materials and structures, Journal of Materials Research and Technology, 9(6), 15705-15738.

Li, T. and Harris, D.K. 2021. Mapping textual descriptions to condition ratings to assist bridge inspection and condition assessment using hierarchical attention, Automation in Construction, 129, 103801.

Liu, H. and Zhang, Y. 2020. Bridge condition rating data modeling using deep learning algorithm, Structure and Infrastructure Engineering, 16(10), 1447-1460.

Mandrekar, J.N. 2010. Receiver operating characteristic curve in diagnostic test assessment, Journal of Thoracic Oncology, 5(9), 1315-1316.

Mehlig, B. 2022. Machine learning with neural networks: an introduction for scientists and engineers, Cambridge University Press, Cambridge, UK.

Neimz, P., Teishcinger, A., and Sandberg, D. 2023. Modeling the mechanical behavior of wood materials and timber structures, Springer Handbook of Wood Science and Technology, Springer, Cham, Switzerland.

Neisen, M. and Geraskin, P. 2022. Improved credit default prediction using machine learning and its impact on risk-weighted assets of banks, Journal of AI, Robotics & Workplace Automation, 1(4), 1-14.

Nowak, A.S. 1999. Calibration of LRFD bridge design code (NCHRP 368), Transportation Research Board, Washington, DC.

Nowak, A.S. and Collins, K.R. 2013. Reliability of structures, CRC Press, Boca Raton, FL.

Pahnabi, N., Schumacher, T., and Sinha, A. 2024. Imaging of structural timber based on in situ radar and ultrasonic wave measurements: a review of the state-of-the-art, Sensors, 24(9), 2901.

Palma, P. and Steiger, R. 2020. Structural health monitoring of timber structures- Review of available methods and case studies, Construction and Building Materials, 248, 118528.

Pournou, A. 2020. Biodeterioration of wooden cultural heritage: organisms and decay mechanisms in aquatic and terrestrial ecosystems, Springer, Cham, Switzerland.

Rashidi, M., Hoshar, A.N., Smith, L., Samali, B., and Siddique, R. 2021. A comprehensive taxonomy for structure and material deficiencies, preventions and remedies of timber bridges, Journal of Building Engineering, 34, 101624.

Reinprecht, L. 2016. Wood deterioration, protection and maintenance, Wiley-Blackwell, Hoboken, NJ.

RIDOT. 2022. Bridge load rating guidelines, Rhode Island Department of Transportation, Providence, RI.

Ritter, M.A. 1990. Timber bridges: design, construction, inspection, and maintenance, United States Department of Agriculture Forest Service, Washington, D.C.

Saad. K. and Lengyel, A. 2022. Strengthening timber structural members with CFRP and GFRP: a state-of-the-art review, Polymers, 14(12), 2381.

USDA. 2010. Wood handbook: wood as an engineering material, Forest Products Laboratory, US Department of Agriculture, Madison, WI.

TFEC. 2018. Seasoning checks in timbers, Bulletin No. 2018-10, Timber Frame Engineering Council, Alstead, NH.

Walker, M. 2022. Data cleaning and exploration with machine learning, Packt Publishing, Birmingham, UK.

White, R.H. and Ross, R.J. 2014. Wood and timber condition assessment manual: second edition. General Technical Report FPL-GTR-234, U.S. Department of Agriculture, Madison, WI.